UiT
THE ARCTIC
UNIVERSITY
OF NORWAY

Faculty of Science and Technology
Department of Physics and Technology

Fast Estimation of Ocean Background Reflectivity in Synthetic Aperture Radar Images

Tina Eliassen Nylehn

Master thesis in Energy, Climate and Environment, EOM-3901 - June 2015

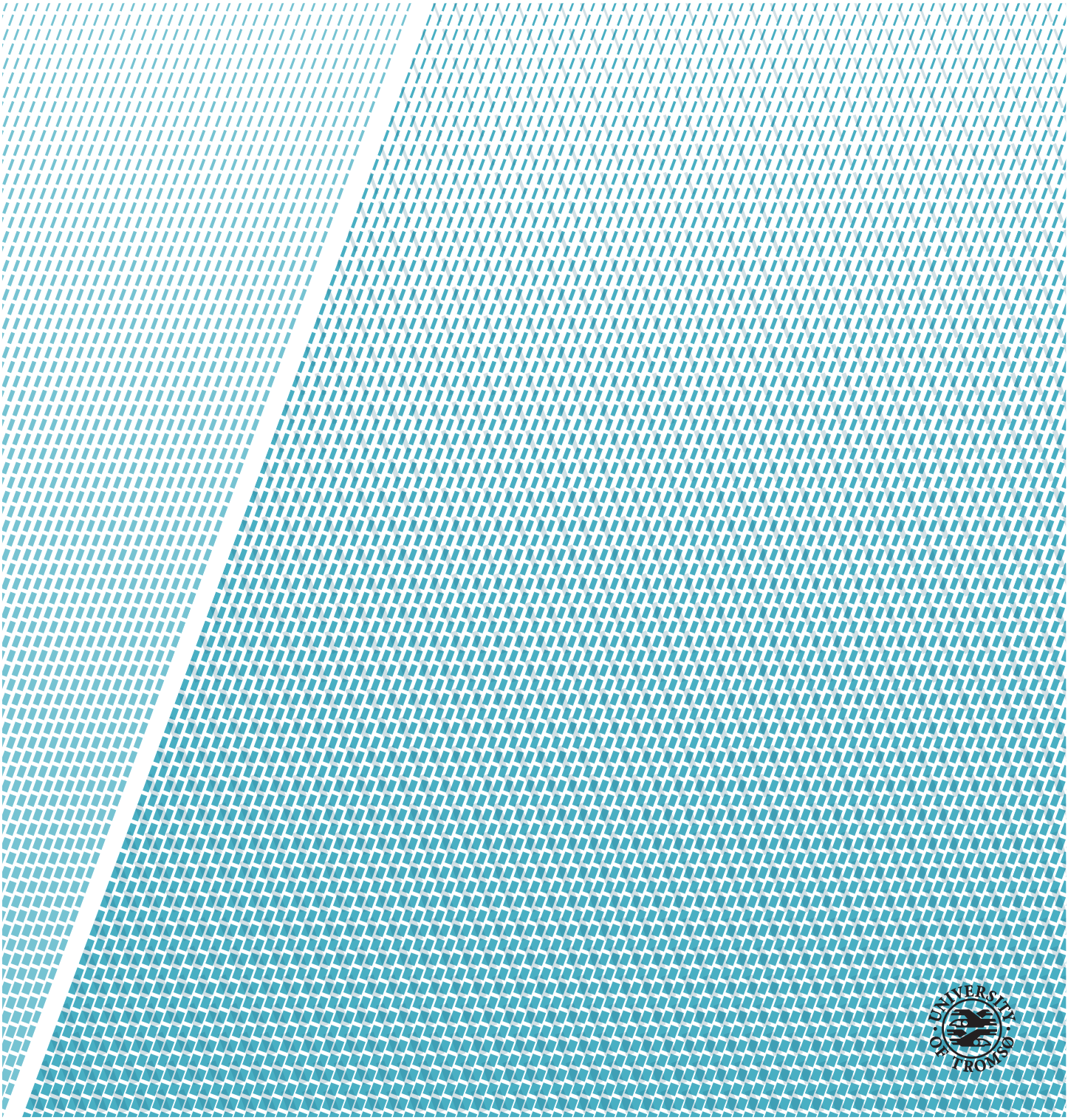

Abstract

Several ship detection algorithms have been developed over the years, where some of the most commonly used are the constant false alarm rate (CFAR) algorithms. There are challenges to the existing algorithms, both when it comes to processing time and difficult scene situations, such as heterogeneous ocean clutter and multiple targets. Existing algorithms that are equipped to handle situations where clutter edges and multiple targets are present, will require significantly increased processing time.

The goal of this thesis is to present a new fast method to estimate the underlying radar reflectivity from a speckled SAR image. The aim is to recover the mean intensity, which is a key parameter in statistical models of SAR intensity measurements over ocean. The estimation of the mean intensity should be fast and robust, in the sense that it handles heterogeneous clutter edges and the presence of multiple targets. The result from the presented algorithm is meant to be an input parameter for current ship detectors.

The steps of the intended algorithm is to take advantage of a nonuniform FFT (NFFT) to truncated SAR data, which will result in frequencies on a regular grid. Next, a lowpass filter will be applied in order to suppress speckle present in the image. Finally, an inverse transformation will be utilized and an estimated mean intensity can be recovered. Thus, a threshold can be determined based on this mean value. Because the NFFT did not provide the desired results, it was not possible to present a complete algorithm.

Acknowledgements

First I would like to thank my supervisors; Stian Normann Anfinsen (UiT), Lars-Petter Gjøvik (KSPT), and Ole Morten Olsen (KSPT). Thank you for your contagious enthusiasm, as well as for your advice, guidance and discussions, especially in the final weeks, when things did not go completely as I had hoped.

I would also like to thank Kongsberg Spacetec AS for a friendly working environment, as well as providing me with an office and excessive amounts of coffee.

Without the amazing girls of EKM 09 and Martine, my student carrer would not have been as fun and inspiring. Marianne and Kirsti, studying abroad for a semester with you in Hong Kong was an adventure and I cherish the memories.

To my family in Harstad and my best friend Annette in Maastricth, thank you for your love and support, and for always being just a phone call away.

Tina Eliassen Nylehn
Tromsø, May 2015

Contents

List of Figures

List of Tables

1 Introduction

Ship detection is an important marine application of synthetic aperture radar (SAR) images. It is used to monitor ship traffic for the purpose of enhanced marine safety and to better control fisheries, pollution, and illegal activities like smuggling and piracy. Being able to detect ships might also be an advantage when it comes to assessing oil spills, as the two may be connected in some situations. It is desirable for a ship detection to bring forth a result as fast as possible. By doing so, organizations such as the coast Guard may be notified, and appropriate measures can be taken.

There are a wide variety of advantages of using SARs to monitor ship traffic. SAR is operational both day and night and it is unaffected by weather conditions. Wide coverage is provided, which will result in a global perspective, and access to areas that are usually difficult to come by will be made possible with the use of SAR.

Several ship detection algorithms have been developed over the years, where some of the most commonly used are the constant false alarm rate (CFAR) algorithms. The CFAR principle is used in a number of algorithms, such as conventional algorithms like the cell-averaging CFAR (CA-CFAR) and order-statstic CFAR (OS-CFAR) and in more recent algorithms like the truncated statistics CFAR (TS-CFAR) developed by [1]. There are challenges to the existing algorithms, both when it comes to processing time and difficult scene situations, such as heterogeneous ocean clutter and multiple targets. Existing algorithms that are equipped to handle situations where clutter edges and multiple targets

are present, will require significantly increased processing time. This thesis seeks to improve a stage in ship detection algorithms that traditionally demands a great deal of processing time, especially in the presence of difficult scene situations.

The thesis is characterized by the fact that the technical developments were not met. This is because an essential part of the proposed algorithm provided undesirable results.

1.1 Motivation and contribution

As mentioned in the previous section, a ship detection algorithm should be implemented to run as fast as possible and at the same time handle difficult scene situations. In ship detection, it is common to make an assumption about the statistical distribution of the ocean background. Thus, the approach to ship detection is usually composed of two main stages: 1) estimating model parameters; 2) the detection itself, that is, hypothesis testing based on the assumed model. The estimation of the ocean background, specifically estimation of the parameters in the statistical distribution models, is the part of ship detection that is most time consuming. Therefore, the concern of this thesis will be on the first stage, mainly, estimating model parameters.

The goal of this thesis is to present a new fast method to estimate the underlying radar reflectivity from a speckled SAR image. The aim is to recover the mean intensity, which is a key parameter in statistical models of SAR intensity measurements over ocean. The estimation of the mean intensity should be fast and robust, in the sense that it handles heterogeneous clutter edges and the presence of multiple targets, situations that are often challenging for existing ship detectors. The result from the presented algorithm is meant to be an input parameter for current ship detectors.

The outline of the proposed algorithm is presented in figure 1.1. The aim is to take advantage of a nonuniform fast Fourier transform (NFFT) to truncated SAR data, in order to obtain frequencies on a regular grid. Once the output is retrieved, a lowpass filter is applied in order to suppress speckle present in the image. After the lowpass filter has been applied and speckle is removed, and inverse transformation is utilized and the mean intensity can be recovered from the estimated radar cross section. In the truncation process, high intensity pixels belonging to the ocean background will also be removed, which will cause the recovered mean intensity to be underestimated. Therefore, it is necessary to compensate for the energy lost in this process.

Because the new algorithm to be presented is based on the recently developed algorithm [1], some of the former CFAR algorithms will be presented, as well as some important theory on ship detection. Basic SAR theory, in addition to methods needed to understand and later execute future algorithms will also be reviewed.

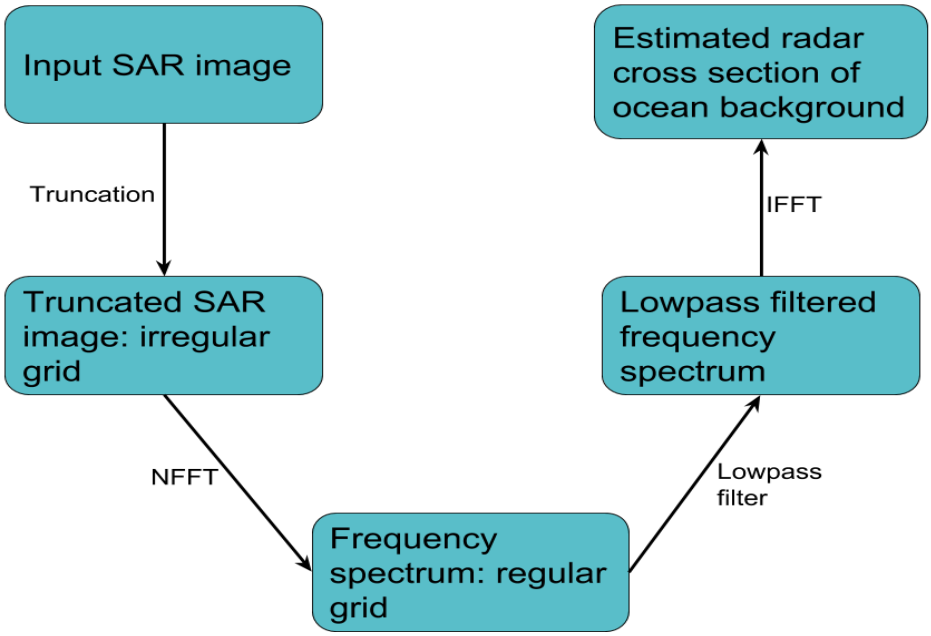

Figure 1.1: *Outline of proposed algorithm.*

The objectives of this thesis are:

- Study the frequency threshold for lowpass filtering in the frequency domain.
- Review NFFT theory and study existing NFFT software.
- Investigate the NFFT's ability in regards to SAR images with irregular grids.
- Discuss how to compensate for the energy removed in the truncation process.

1.2 Structure of the thesis

This thesis starts off by reviewing various aspects of synthetic aperture radar (SAR) theory in chapter 2, such as imaging geometry, resolution, speckle and radar cross section (RCS).

Chapter 3 addresses how ocean clutter and ships are imaged by SAR and reviews essential detection theory. One of the most common ship detectors, the CFAR algorithm, will also be introduced. Traditional CFAR detectors such as CA-CFAR and OS-CFAR will be presented, as well as a newly propsed TS-CFAR algorithm.

Chapter 4 introduces theory on various matters, such as lowpass filters, evaluation measures, and the nonuniform NFFT. All of these will be utilized in the desire to reach the goals set for this project.

Chapter 5 presents the two datasets that will be considered in this thesis, one consisting of simulated data and one acquired from Konsberg Spacetec AS (KSPT) consisting of real SAR data. The Radarsat-2 satellite will also be presented.

Chapter 6 provides results from the different elements of this thesis. First, a frequency threshold will be discussed and set, before the performance evaluation of the NFFT in regards to truncated data is discussed. This chapter also includes a few sections on troubleshooting and analysis of issues that arose when dealing with the NFFT.

The conclusion and recommendations for future work is presented in chapter 7.

2

Synthetic Aperture Radar Imaging

In remote sensing there are two types of sensors to consider. A passive sensor gathers energy from external sources, for example energy reflected from the sun or the Earth's own thermal energy. Active sensors provide their own illumination source, that is, the sensor generates the energy itself before emitting the radiation and then detecting the reflected energy from the surface [2]. For the purpose of this project, the focus will be on a synthetic aperture radar.

A synthetic aperture radar (SAR) is an active sensor that operates in the microwave region of the electromagnetic (EM) spectrum, with wavelengths ranging from 1 mm to 1m and frequencies ranging from 0.3 GHz to 300 GHz. For the most part of the microwave region, the atmosphere is transparent and will therefore be unaffected by scattering and absorption mechanisms. This means that it is not affected by weather conditions and it is also independent of solar illumination [2].

In SAR theory, the properties of the EM spectrum is utilized. When the wave interacts with the surface, its properties will change. This change is dependent on the properties of the target, such as geometry and physical and chemical structure, properties of the sensor platform, and properties of the incoming wave. Information about objects or features on the surface is transmitted to the sensor by EM energy can be contained in the frequency content, intensity

or polarization properties of the EM wave [2].

2.1 Synthetic Aperture Radar Principles

A synthetic aperture radar transmits coherent EM pulses towards a surface of targets. When the EM radiation interacts with the surface, the radiation is absorbed, transmitted or reflected, dependending on the surface properties. The sensor will receive echoes from a target as long as it is within the (azimuth) footprint or antenna pattern. This is illustrated in Figure 2.1, where transmitted pulses will be recorded by a moving sensor from a target A from the moment it enters the beam until it leaves it. In Figure 2.1, B represents the synthesized antenna length [3][4].

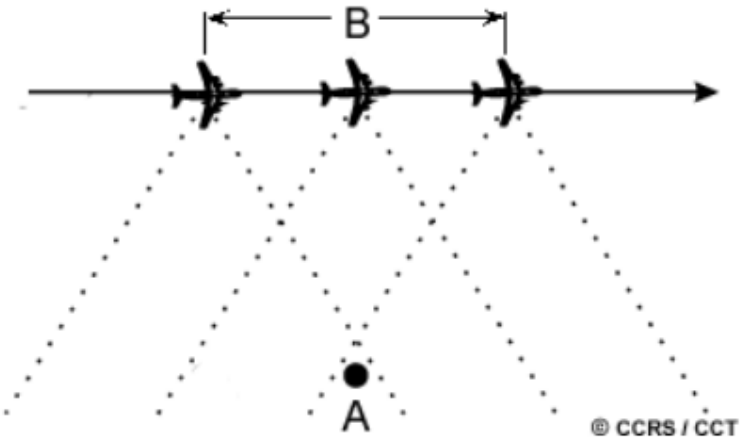

Figure 2.1: *Illustration of how echoes are received from a target A as long as it is within the antenna pattern. The synthesized antenna length is given by B. (figure from [4])*

The reflected EM energy is sent back to the sensor, where the received signal will be segmented into sections in order to create a two-dimensional signal. These sections are combined to form a matrix. The first dimension of the matrix, and thus the resulting image's x-axis (range), is parallel to the radar beam and perpendicular to the movement of the imaging platform. There is a time delay between the echoes that are backscattered from the various surface components. This time delay is applied when separating the incoming radar echoes. The second dimension of the matrix, and thus the resulting image's y-axis (azimuth) corresponds to the direction parallel to the movement of the imaging platform. In order to separate the surface pixels in this direction, the Doppler history is utilized [3][5].

2.1.1 Imaging geometry

Figure 2.2 illustrates the SAR geometry. The pulses are sent out perpendicular to the sensor's flight direction. The along-track direction parallel to the flight direction is called azimuth, while the across-track direction perpendicular to the flight direction is called range.

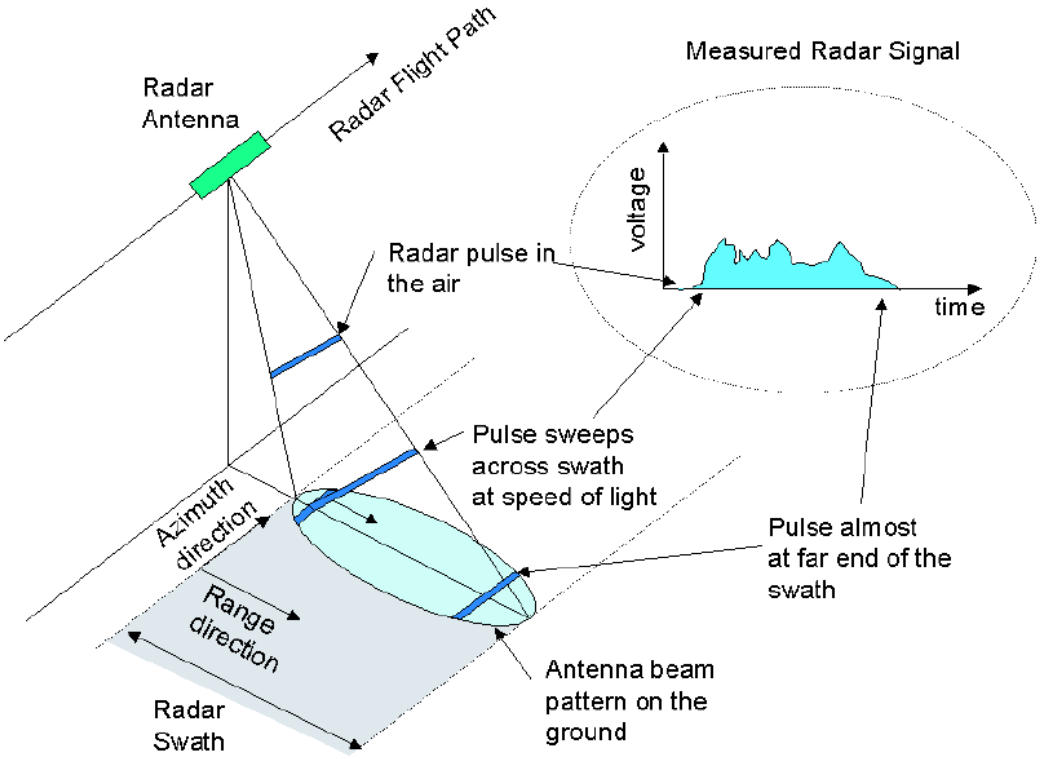

Figure 2.2: *Illustration of SAR geometry (figure from [6])*

Figure 2.3 illustrates more important aspects of the SAR geometry. The incidence angle (A) is the angle between the radar beam and a line perpendicular to the ground surface. The look angle (B) is the angle at which the radar looks at the ground surface. The ground range (D) is the true horizontal distance, while the slant range (C) is the distance measured along the line of sight between the antenna and the surface [4]. In figure 2.3, note that $A \neq B$, as the Earth is curved (more notable for spaceborne SAR).

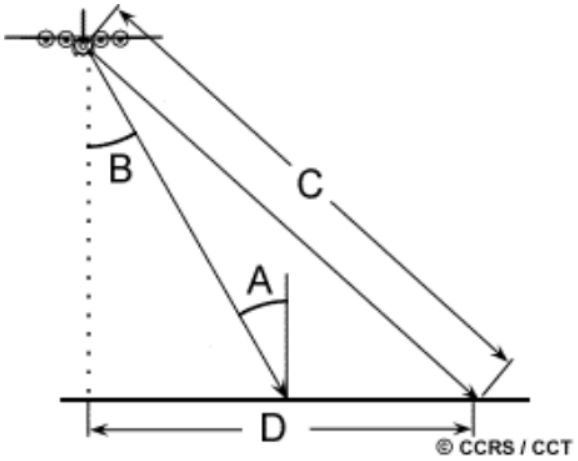

Figure 2.3: *Illustration of SAR geometry. Letters A-D illustrate incidence angle, look angle, slant range, and ground range, respectively. Note that $A \neq B$ due to curved Earth geometry (figure from [4]).*

2.1.2 Spatial Resolution

This section discusses resolution, which identifies the smallest object that can be detected in an image [2]. It is important to separate azimuth and range resolution as they are defined differently and depend on different parameters.

Range resolution

The range resolution is dependent on the emitted pulse. That is, two objects can only be distinguished in the range direction if their returning pulses arrive at different times. To be more precise, the distance between two targets on the ground need to be greater than half the pulse length. Therefore, it is clear that a shorter pulse length will result in a better range resolution [2]. It is important that the received signal is strong enough to discriminate it from the noise floor. Therefore, an increased amplitude is needed and this requires more power in the transmitter. The solution is to use a chirp pulse, which is a frequency modulated signal with an effective pulse length reduced from microseconds to nanoseconds [3].

The resulting slant range resolution is given as [3]

$$\Delta R_s = \frac{c}{2}\tau \tag{2.1}$$

while the resulting ground range resolution is given as [3]

$$\Delta R_g = \frac{c\tau}{2\sin\theta} \tag{2.2}$$

where c is the speed of light, θ is the incidence angle, and τ the chirp pulse length.

Azimuth resolution

The azimuth resolution refers to the minimum distance two points on the ground (along an azimuth line) can be separated by, and still be distinguishable. This distance is equal to the beam width D_A, which means that two objects on the ground can only be identified if they are not in the footprint at the same time.

The real aperture radar (RAR) resolution is given as [6]

$$\Delta x = \frac{\lambda h}{D_A \cos\theta} \tag{2.3}$$

where λ is the wavelength, h is the height above the surface, θ is the incidence angle, and L is the antenna length. Thus, by evaluating equation (2.3), it is clear that the azimuth resolution is proportional to the distance from sensor to target and inversely proportional to the antenna length. The distance from antenna to target is very large and increasing the antenna length substantially will prove problematic. The solution is to use SAR, where an increased antenna length is synthesized during post-processing. This is done using the Doppler history of the collected signals, and the resulting azimuth resolution becomes [7]

$$\Delta x = \frac{D_A}{2}. \tag{2.4}$$

The SAR azimuth resolution is no longer dependent on the distance from the antenna to the target.

2.1.3 Radar equation

The radar equation describes the relationship between the transmitted power P_t and the received power P_r at the sensor. The equation is derived by regarding the ground as an antenna that can transmit and receive power. Before the radar equation is derived, some parameters must be defined [2]:

- A_g - effective area of the ground

- A_e - effective area of the antenna
- G_g - gain factor of the ground
- G_t - gain factor of the antenna
- P_r - received power at the sensor
- P_t - transmitted power from the sensor with gain G_t and effective area A_e
- P_g - received power at the ground within an area A_g
- $P_{g'}$ - power reradiated from the ground with gain G_g
- r - distance between the ground and the antenna

As stated, the ground is regarded as an antenna and thus, the power received within an area A_g on the ground is given as

$$P_g = \frac{P_t}{4\pi r^2} G_t A_g \tag{2.5}$$

The received power at the actual antenna, given that the ground transmits $P_{g'}$ with antenna gain G_g, is given by

$$P_r = \frac{P_{g'}}{4\pi r^2} G_g A_e \tag{2.6}$$

Thus, the ratio P_r and P_t can be found, i.e.

$$\frac{P_r}{P_t} = \left[\frac{P_{g'}}{P_g} G_g A_g\right] \frac{G_t A_e}{(4\pi r^2)^2} \tag{2.7}$$

The expression within the brackets in equation (2.7), is defined as the radar cross section (RCS) and it is denoted by σ, with units of m^2. A_e can be expressed as

$$A_e = \frac{\lambda^2}{4\pi} G_t \tag{2.8}$$

where λ is the wavelength of the radiation. Thus the resulting radar equation that describes the received radiation P_r when P_t is the transmitted radiation per unit area is [8]

$$P_r = \frac{\sigma \lambda^2 G_t^2}{(4\pi)^3 r^4} P_t \tag{2.9}$$

Radar Cross Section (RCS)

The radar cross section (RCS) provides information on how detectable a surface or target is to the radar. When energy is transmitted from the sensor, a specific energy density is incident on the surface. The surface will scatter the received energy, in which some of the energy is scattered back towards the sensor. The RCS describes the ratio between the energy density scattered towards the sensor and the incoming energy density [9][10]. Often, the normalized radar cross section is used:

$$\sigma^0 = \frac{\sigma}{A_g} \tag{2.10}$$

The RCS depends on numerous factors, and some of them are [2]:

- Surface roughness
- Dielectric properties
- Wavelength
- Polarization
- Incidence angle

A surface's electrical properties can be represented by the dielectric constant, which describes how well a surface is able to store and transmit electrons. Generally, a higher moisture content will give rise to a larger dielectric constant (water $\approx$ 80) [2]. Polarization and surface rurface roughness will be introduced in the following sections.

2.1.4 Polarization

EM waves have many properties that are important in remote sensing. Their polarization is one of them. EM waves consists of perpendicular electric and magnetic fields that oscillate in a synchronized manner. The polarization of a given EM wave is related to the orientation of the electric field [6]. In traditional remote sensing and SAR, the transmitted EM waves and the received EM waves are usually horizantally or vertically polarized (see illustation in figure 2.4). There are four different channels commonly used in SAR:

- HH - transmitted and received EM wave are both horizontally polarized
- HV - transmitted EM wave is horizontally polarized and received EM

wave is vertically polarized

- VV - transmitted and received EM wave are both vertically polarized
- VH - transmitted EM wave is vertically polarized and received EM wave is horizontally polarized

The HH and VV channels are usually referred to as co-polarized, while VH and HV are usually referred to as cross-polarized [11]. Different polarization channels will interact with the surface and targets differently, and this fact is exploited in remote sensing. The channel used affects the backscattered signal and what information can be obtained from the surface.

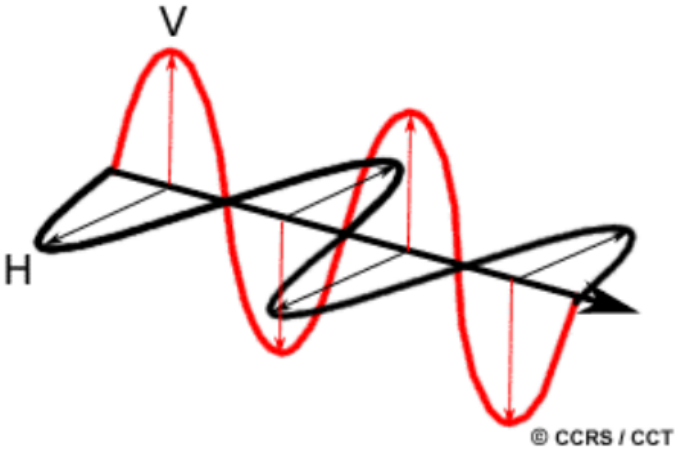

Figure 2.4: *Illustration of a horizontally polarized EM wave(black) and a vertically polarized EM wave(red) (figure from [4]).*

Satellites can have different types of polarization systems; a single polarization (single-pol) system, a dual polarization (dual-pol) system and a quadrature polarization (quad-pol) or full polarimetric system [11]. A single polarization system is a system that transmits and receives on one polarization channel (H or V). Therefore, there are four possible channels for a single-pol system: {HH}, {HV}, {VV}, and {VH}. A dual-pol system is a system that transmits on one polarization channel and receives on two polarization channels. This yields two possible channel combinations: {HH, HV} or {VV, VH}. A full-pol or quad-pol system is a system that both transmits and reveives on two polarization channels. Thus, all channels are recorded: {HH, HV, VV, VH} [11].

Whether to use a single, dual or full polarimetric system depends on what the objective of the mission is. For example, if one wants to survey a marine area, one might want to choose a single or dual polarimetric system, as these will provide a larger swath width than the full polarimetric system.

2.2 Speckle and multilooking

An inherent property in all SAR measurements is a type of noise-like feature called speckle. In a SAR image, this feature will appear as a grainy salt and pepper pattern. Every pixel in a SAR image represents an area on the ground which is often referred to as a resolution cell. Within this resolution cell there are numerous scatterers. The returned signal from the resolution cell will consist of echoes from all the scatterers within the given cell. The reflected EM waves from the different scatterers will have different phase and amplitude and the speckle effect is caused by coherent interference of these waves [11]. The phase of each of the scattering points is related to the distance between the antenna and the scattering point [6]. Because the scatterers are located randomly within the resolution cell, this distance will vary. Constructive interference results in a strong signal, while destructive interference results in a weak signal. The previous mentioned aspects of the speckle effect and why it occurs are summed up in figure 2.5.

Speckle is in fact the signal itself and can be thought of as multiplicative noise where the backscattered intensity image at a given time t and position $\mathbf{x}$ can be written as [12]

$$I(\mathbf{x}, t) = I_0(\mathbf{x}, t)\eta(\mathbf{x}, t) \tag{2.11}$$

where η represents the speckle and I_0 is the unspeckled radar reflectivity/radar cross section.

Interpretation and analysis of SAR images will prove difficult because of speckle. For instance, the effectiveness of image segmentation algorithms will be reduced, and therefore it is desirable to reduce the speckle [11]. Numerous speckle filters have been developed and evaluated. Speckle reduction can be executed after image formation by applying a filter that will smooth the image. It is also possible to reduce speckle before the image is formed with a process called multilooking. Suppressing speckle can be done in both the spatial or the frequency domain [13][14].

Multilooking can be done both in the frequency domain and in the spatial domain. Multilooking in the frequency domain refers to the process of dividing the aperture length into L segmented looks. The L looks, which are independently processed and averaged to form an intensity image or an amplitude image, are summed together in order to create an L-look image. This process will reduce the signal variations and thus the speckle (the standard deviation of the speckle is reduced by a factor of $\sqrt{L}$), but at the expense of the azimuth resolution, which will be degraded by a factor L [11]. Multilooking in the spatial domain is done by applying a moving average filter to the SAR image during postprocessing [4].

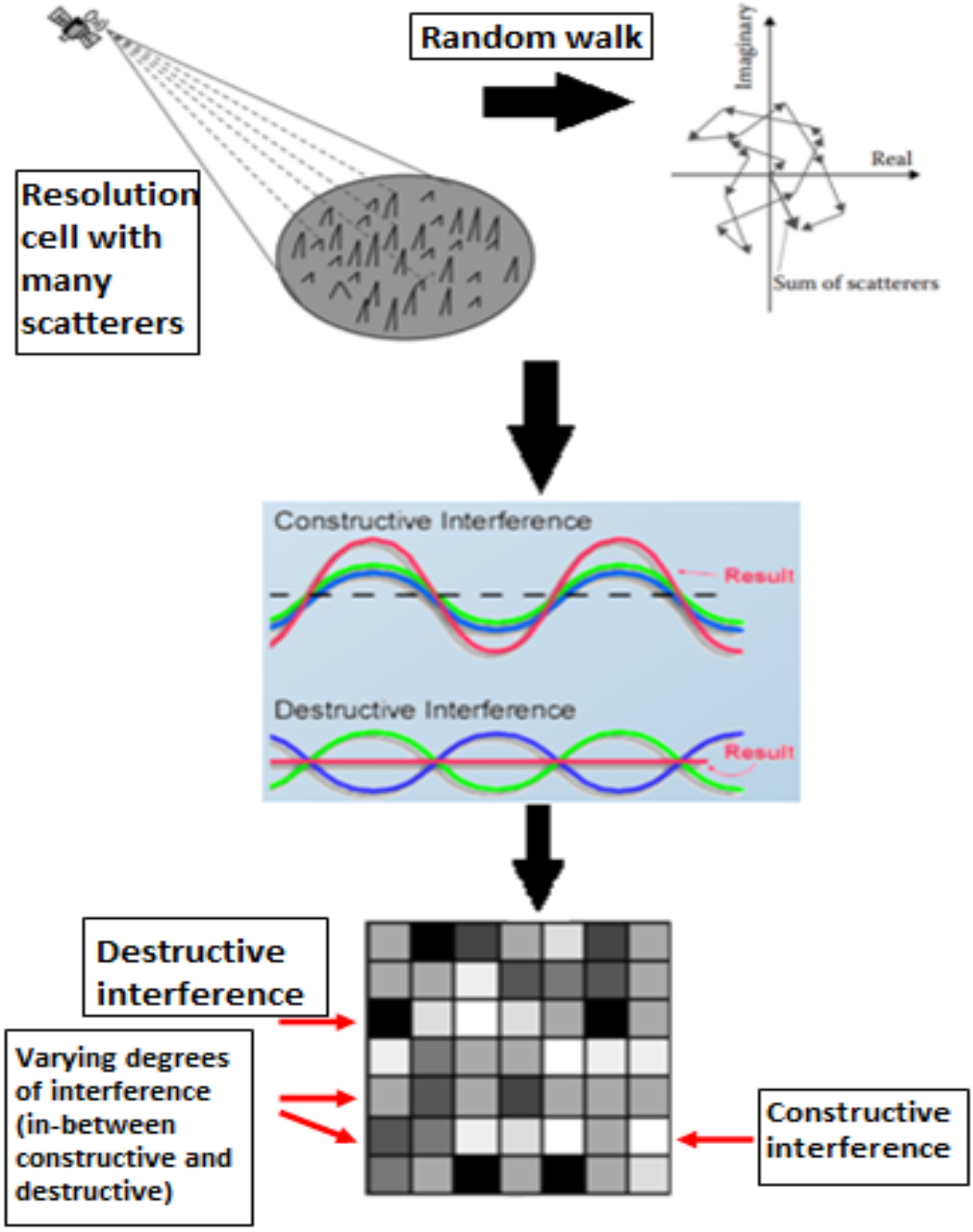

Figure 2.5: *Illustration of the speckle effect and why it occurs. An area on the ground (resolution cell) will contain numerous scatterers. The returned signal from the resolution cell will consist of echoes from all the scatterers. The reflected EM waves from the different scatterers will have different phase and amplitude (random walk model). The speckle effect is caused by coherent interference of the EM waves from the different scatterers (figure from [4] and [11]).*

2.3 Scattering Mechanisms

When an EM wave interacts with the surface and its targets, many parameters need to be consider in order to explain the returned backscatter at the antenna. It is not only dependent on the properties of the EM wave itself, like fequency, polarization and wavelength, but also the geometry of the surface, the incidence angle and the dielectric properties of the surface [4]. The three main types of scattering mechanisms that are used to understand the interactions between the incident EM wave and the surface targets are surface or single-bounce scattering, dihedral or double-bounce scattering, and volume scattering.

2.3.1 Surface scattering

Surface scattering occurs when the incident EM wave has been dispersed only once by the boundary between two media. There are three different scenarios in which this may happen, and they are highly dependent on the roughness of the surface. Because the surface scatters the incoming EM radiation differently for varying degree of roughness, it is neccessary to understand how roughness is defined. One criterium used for defining roughness is the Rayleigh criterium, which states that a surface is considered smooth if the phase difference between two scattered waves is less than $\pi/2$ (see figure 2.6).

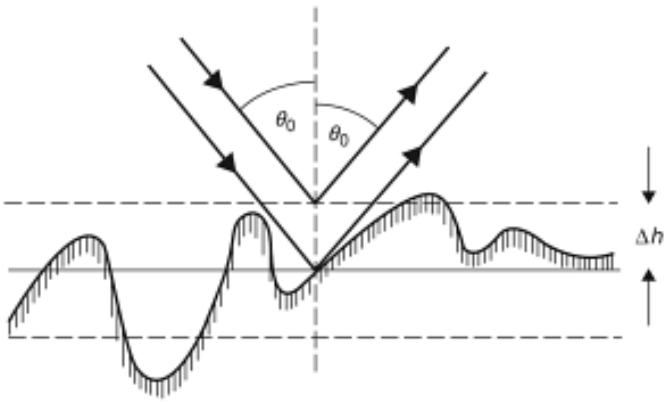

Figure 2.6: *Illustration of the parameters needed to define roughness (Rayleigh criteria). Phase differnece between the two scattered waves depends on the wavelength (λ), the incidence angle (θ_0), and the height standard deviation (Δh) (figure from [15]).*

Therefore, a surface is defined as smooth if the following criterium is true

[6][7]

$$\Delta h < \frac{\lambda}{8 \cos \theta_0} \tag{2.12}$$

where Δh is the standard deviation of the surface height, λ is the wavelength, and θ is the incidence angle.

A smooth surface will reflect incident radiation in a specular manner, where the reflection angle is equal to the incidence angle of the incoming EM wave. This results in little or no energy being returned to the radar, which is why smooth surfaces will appear as dark-toned aras in an image [4].

A Lambertian surface scatters the EM energy equally in all directions. A very rough surface may act as a Lambertian surface or at least approximately equal to one. Because of this, a much larger portion of the EM energy will be returned to the radar compared to the energy returned from a smooth surface. Therfore, very rough surfaces will appear lighter in an image. The roughness of the surface is usually dependent on the incidence angle. Generally, the surface will appear to be more rough with increasing incidence angle. For a very rough surface, which is perfectly diffusive, the backscattered radiation will not depend on the incidence angle [4].

A surface that is slighty rough, will experience both specular reflection and diffusive scattering. An illustration of the three different scenarios of surface scattering can be seen in figure 2.7 below.

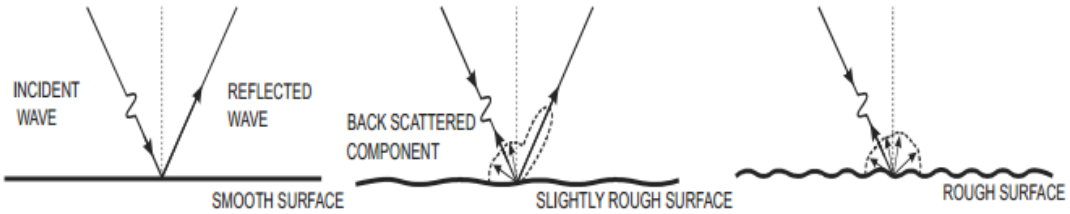

Figure 2.7: *Surface scattering from a smooth surface, a slightly rough surface, and a rough surface (figure from [16]).*

Bragg scattering

There is a fourth scattering scenario within the surface sattering category called Bragg scattering, which often applies to ocean surfaces. Bragg scattering occurs when the wavelength of the incident EM wave is resonant with the wavelength of the ocean facet. The Bragg model assumes that the backscattered energy is primarily a result of the ocean surface spectral component resonating with the

incident EM waves.

The Bragg wavelength λ_B of the ocean which causes Bragg resonance is given by

$$\lambda_B = \frac{n\lambda_R}{2\sin\theta} \tag{2.13}$$

where n is the order of the resonance, λ_R is the radar wavelength, and θ is the incidence angle (see figure 2.8). In equation 2.13, it is assumed that the travel direction of the the ocean waves is in the radar line of sight [17]. The resonant waves are dependent on both the wavelength of the incidence wave and the incidence angle, as can be seen in the equation above.

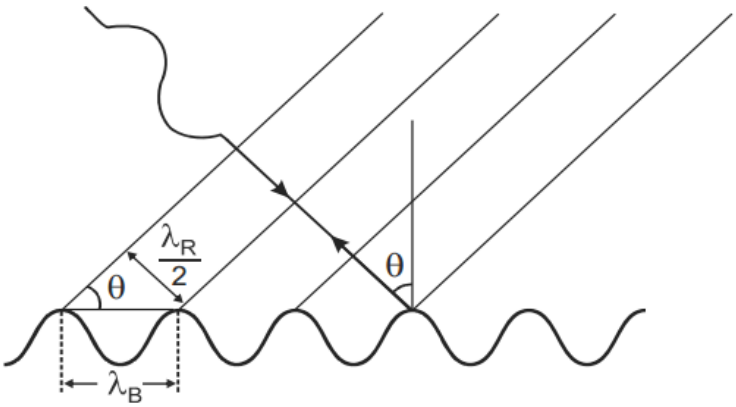

Figure 2.8: *Bragg resonant scattering on sea waves where λ_B is the bragg wavelength, λ_R is the wavelength of the incidence EM waves, and θ is the incidence angle (figure from [16]).*

The ocean surface contains so-called capillary waves with lengths around 2 cm and short gravity waves with lengths around 50 cm. It is these two types of waves that are known to cause Bragg scattering. For incidence angles above 20 degrees, the ocean surface scattering mechanism will primarily be Bragg scattering. The backscatter from the ocean is highly dependent on the ocean surface winds. Higher wind speeds yield a rougher ocean surface, which will increase the amplitude of the resonant waves causing Bragg scattering. Thus, the resulting radar backscatter will be greater [17].

2.3.2 Double-bounce scattering

Double-bounce scattering occurs when the incidence wave is scattered twice when interacting with the surface (see figure 2.9). Features on the ground that have two (or more) perpendicular surfaces will give rise to double-bounce scattering. This will result in a return at the radar that contains high energy, which in turn will cause bright areas in an image [17]. Typical examples of features that cause double-bounce scattering are buildings, streets, bridges and ships on water.

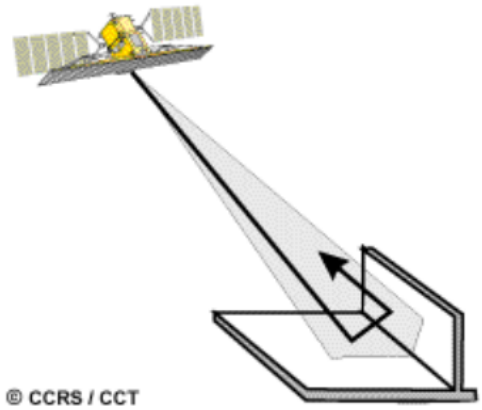

Figure 2.9: *Illustration of double-bounce/dihedral scattering (figure from [4]).*

2.3.3 Volume scattering

The last scattering mechanism to be considered in this thesis is volume scattering. Volume scattering occurs within inhomogeneous bulk materials that contain dielectric properties that vary locally. Volume scattering will only occur when the incidence wave is able to penetrate the aforementioned material. Whether or not the wave is able to penetrate depends on both the wavelength of the incidence wave and the dielecric properties of the medium [18]. Volume scattering may result in both an increase and a decrease of the brightness in an image, depending on how much of the energy is scattered out of the volume and back to the radar [17]. Tree canopies is one example where volume scattering occurs.

3

Ship Detection

The intended application area for the method developed in this project is ship detection. Ship detection is a very effective method in monitoring maritime traffic, such as fishing activites, pollution from ships, and illegal operations where ships are involved, such as smuggling or piracy [19]. The current chapter contains information on how ships and ocean clutter is imaged by SAR. The two major challenges when it comes to ship detection is heterogeneous ocean clutter and the presence of multipe targets. The method developed in this project will hopefully handle these two issues well. The ship detection algorithms that will be reviewed in this chapter are different constant false alarm rate (CFAR) algorithms, where the main focus will be on the CFAR algorithm based on truncated statistics, propsed by [1]. These algorithms are amongst the most commonly used ship detection algorithms.

3.1 SAR imaging of the ocean

An essential topic of this thesis is ship detection and important theory aspects surrounding the subject. In ship detection, the ocean will act as the background and it is therefore important to know how it is imaged by SAR. The ocean backscatter will depend on several different factors, that is, parameters related to both sensor properties and surface characteristics. Roughness and the dielectric constant are parameters related to the surface, while polarization and incidence angle are examples of parameters related to the radar.

Water has a high dielectric constant with respect to air, and the contrast is the reason why the radar only sees the top surface layer of the ocean. In other words, the penetration depth of the ocean surface is minor. The ocean reflects microwaves well, resulting in a generally low backscatter. SAR images of ocean areas will therefore appear dark. In section 2.3.1, Bragg scattering was discussed. Bragg scattering is the dominant scattering mechanism on the ocean surface for incidence angles above 20°, which is where operational SAR systems generally operate [17]. As can be seen in equation 2.13, the resonant wavelengths depend on both the wavelength of the incoming EM wave and the incidence angle, which in turn will affect the ocean backscatter.

The ocean surface will have a varying degree of smoothness, which results in varying backscatter. For smooth surfaces, there will be little or no backscatter, only specular reflection, and the ocean will appear dark in SAR images. This means that it will be extremely hard to deduce surface properties for very smooth surfaces. Therefore, in order to obtain some information about the ocean, it is desirable for the ocean not to be completely smooth. However, in cases where the ocean is very smooth, it will be relatively easy to detect ships or coherent measures. Therefore, such cases are of little interest when improving and developing new robust ship detection algorithms. New detectors are developed with challenging situations such as heterogeneous ocean and mutliple targets in mind. The surface roughness and how it is defined was discussed in section 2.3.1. It is dependent on the incidence angle and the wavelength of the incoming EM wave in relation to the surface height variation. This fact can be seen in equation 2.12.

As mentioned, it is neccessary for the ocean not to be completely smooth in order to extract some surface characteristics. This means that some wind is neccessary, as the occurence of wind will increase the surface height variations, and thus the perceived roughness. There is a dependence between the backscatter and the wind speed, which for a given radar and incidence angle is as follows

$$\sigma^0 \sim |u_s|^\gamma \tag{3.1}$$

where σ^0 is the normalized radar cross section of the ocean, u_s is the wind speed, and γ is a function of the radar parameters [17]. Thus, stronger winds will result in an increased backscatter. Because of the effect that wind speeds have on the roughness and thus the backscatter, it is possible to extract information about local wind speeds and directions from a SAR image.

Other factors that will have a direct impact on the resulting backscatter from the ocean are radar parameters like polarization, radar frequency, and incidence angle. The ocean backscatter will decrease with increasing incidence angle and this is typically true for the co-polarization channels. The co-polarization channels will have lower sea clutter levels than cross-polarization channels,

with VV clutter levels generally higher than HH clutter levels [20]. The ocean backscatter will decrease with increasing radar frequency.

There are several features and processes that can be observed in SAR images, such as atmospheric winds, storm fronts, heavy rain, ocean swells, ocean currents, bottom topography, sea ice, ships and their corresponding wakes, oil rigs, shoals, and man-made and natural slicks and films [17]. Many of these processes and features might cause problems in ship detection algorithms by way of false alarms, explained further in section 3.5.

3.2 SAR imaging of ships

In SAR images, ships will appear as bright targets on an otherwise darker background [16]. There are many different categories of ships. Some are made of metal, while others might be constructed from wood or fiberglass. Ships that are limited to reside in coastal regions tend to be smaller than ships that travel in open waters far out at sea, and some ships are laden, while others are not. Laden ships will sit lower in the ocean and therefore tend to have a smaller radar cross section. These are just some of the properties that will affect the signature of ships in SAR imagery. The motion effects (speed, roll, and heave) of the ship and its surroundings will also affect how it appears in SAR images. A moving ship will have a corresponding wake, which might help detect it. Also, larger radar cross sections will be observed for ships that travel in the azimuth direction as opposed to other directions [17]. Thus, the backscatter from the ship depends on the size and motion of the ship, its orientation, and its structure and build. Figure 3.1 shows a SAR image containing bright pixels that might be targets or ocean installations. Meteorological and oceanographic phenomena are also visible within the SAR image.

The scattering mechanisms that occur most commonly in relation to ships are surface scattering on for example large metal structures of the ship and double-bounce scattering when the incident wave undergoes two bounces, one on the ocean surface and one on the ship. Multiple bounces might also occur from the ship and the ocean surface. As mentioned in the previous paragraph, the motion of the ship will affect its backscatter. If a ship is in motion, this might cause distortions in the azimuth direction, for example azimuth blurring due to the ship's pitch and roll movement [16]. The incidence angle, as well as the polarization and the radar frequency will also help determine the backscatter. For example, a ship's backscatter increases with the use of higher frequency SARs [17].

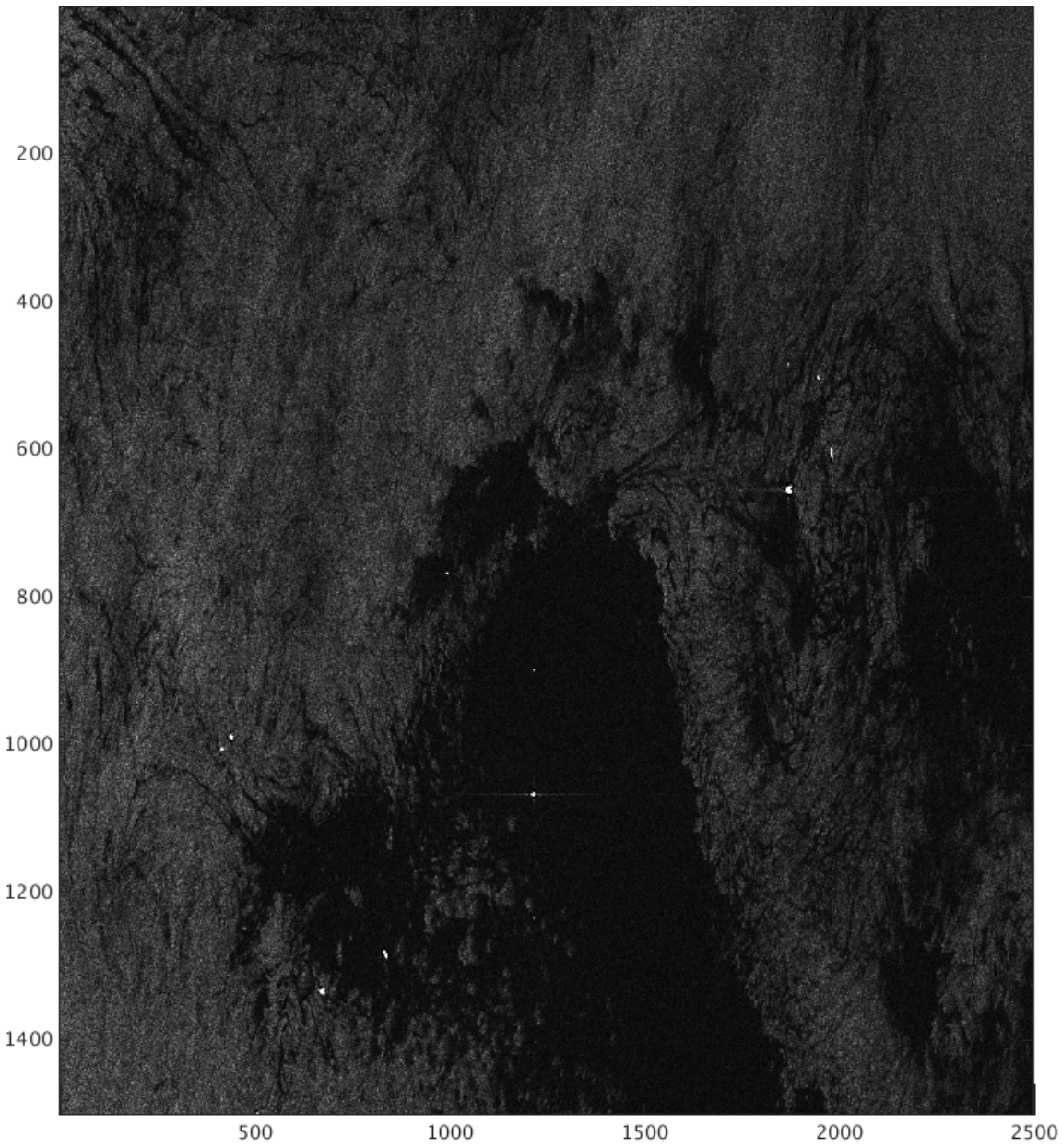

Figure 3.1: *HH-polarization SAR image of an area outside of Nordland, acquired on August 4th of 2012 from the Radarsat-2 satellite. Possible ships and ocean intallations can be seen as bright intensity pixels. Meteorological and oceanographic phenomena are also visible within the image (data acquired from KSPT).*

In ship detection, the contrast between ship and ocean is of great interest. In order to better discriminate the ship from the ocean, a greater contrast is preferred over a lesser one. Because ocean clutter levels are generally higher in the VV channel, one might suggest using the HH channel over the VV channel in ship detection, as this will give rise to a greater ship-sea contrast [20]. The cross-polarization channels will provide even better contrast and in ship algorithm studies, the HV channel with small incidence angles (near range) is sometimes proposed [17].

Other factors that affect ship-to-sea contrast is the state of the ocean, incidence angle, frequency and spatial resolution. Calmer sea states and thus low wind speeds are ideal to increase the contrast. However, ship detection at low wind speed is usually trivial. Thus, the challenge for practical ship detection is to develop methods that handle high winds and inhomogeneous ocean, as well as cases involving multiple targets. A better spatial resolution will also be beneficial in ship detection algorithms, as more ships can be detected. Also, better resolution allows ship classification and characterization after it has been detected, since more pixels are available. With poor resolution, two or more ships might be present in one resoluton cell and therefore, discriminating them from eachother will prove impossible. A large swath width is desirable in ship detection. This will provide greater coverage (global picture) and an opportunity to map ship routes. Choosing larger swath widths as opposed to smaller ones will contribute to a faster way of collecting information from a large area. A large swath width is in contradiction with a better spatial resolution, and in order to decide the tradeoff between them, it is necessary to consider the objective of the SAR image in relation to ship detection.

3.3 Detection Theory

Detection theory refers to observing some data and deciding whether or not an event has occured. In target detection, which is the application area of this study, the event will be the presence of a target. The overall goal of ship detection is to classify pixels as either "target" (ship) or "not-target" (ocean clutter), which is why detection theory can be applied. By observing some SAR data, one wants to decide if a target is present or not. To do so, an hypothesis test is applied to the given data. Thus, a binary hypothesis test is established, i.e. [21]

$$H_0 : \quad \boldsymbol{x} \sim f_{\theta_0}(x) \tag{3.2}$$

$$H_1 : \quad \boldsymbol{x} \sim f_{\theta_1}(x) \tag{3.3}$$

Ocean clutter will have one specific statistical distibution, given by $f_{\theta_0}(x)$, while ships will have another specific statistical distribution, given by $f_{\theta_1}(x)$. Pixel

observations are contained in $\boldsymbol{x}$ and these will be classified as belonging to the distribution of ocean clutter (decide H_0) or the distribution of ships (decide H_1). Thus, the general goal is to observe some data $\boldsymbol{x}$, and design some sort of rule that will decide which hypothesis that best corresponds to that data. However, because it is not possible to model the statistical distribution of ships $f_{\boldsymbol{\theta}_1}(x)$, the hypothesis test is reformulated, i.e.

$$H_0 : \quad \boldsymbol{x} \sim f_{\boldsymbol{\theta}_0}(x) \tag{3.4}$$

$$H_1 : \quad \boldsymbol{x} \nsim f_{\boldsymbol{\theta}_0}(x) \tag{3.5}$$

There are four possible outcomes of the above hypothesis test:

1. "Detection" - a pixel is correctly classified as a ship (H_1 true, decide H_1)
2. "False alarm" - a pixel is classified as a ship, when it in reality is ocean clutter (H_0 true, decide H_1)
3. "Miss" - a pixel is classified as ocean clutter, when in reality, it is a ship (H_1 true, decide H_0)
4. A pixel is correctly classified as ocean clutter (H_0 true, decide H_0)

The performance of a test is typically characterized by assessing the probability of detection and the probability of false alarm. The probability of detection $\left(\mathrm{P}_D\right)$, that is, correctly deciding H_1, is defined as [21]

$$\beta = \int_{\boldsymbol{x} \in R} f_{\boldsymbol{\theta}_1}(\boldsymbol{x}) \, \mathrm{d}\boldsymbol{x} = P_D \tag{3.6}$$

and the probability of false alarms $\left(\mathrm{P}_{FA}\right)$, that is, deciding H_1 when H_0 is true, is defined as [21]

$$\alpha = \int_{\boldsymbol{x} \in R} f_{\boldsymbol{\theta}_0}(\boldsymbol{x}) \, \mathrm{d}\boldsymbol{x} = P_{FA} \tag{3.7}$$

where the different probabilities are illustrated in figure 3.2. The statistical distributions of the "target" (blue) and the "not-target" (red) measurements are depicted, an example threshold is set (dashed line), and regions A (acceptance region) and R (rejection region) are decided based on this threshold. The acceptance region A corresponds to deciding/accepting H_0, while the rejection region R corresponds to deciding H_1 or rejecting H_0.

As mentioned earlier, a decision rule has to be determined. A decision rule that maximizes the probability of detection and minimizes the probability of false alarms is desirable. In a perfect world, there would be no overlap between the

distributions of ships and ocean clutter, and thus, a theshold could be chosen, such that

$$P_D = 1 \qquad P_{FA} = 0$$

A binary hypothesis test of H_0 versus H_1 takes the form [21]

$$\phi(\boldsymbol{x}) = \begin{cases} 1 \sim H_1 & \text{if } \boldsymbol{x} \in R \\ 0 \sim H_0 & \text{if } \boldsymbol{x} \in A \end{cases} \tag{3.8}$$

The test funtion $\phi(\boldsymbol{x})$ equals 1 (choose H_1) if the observation $\boldsymbol{x}$ lies in the rejection region R. If the observation lies in the acceptance region, A, the test function will be equal to 0 (choose H_0). These two regions are described by the threshold, which depends on the desired P_{FA} [21]. The challenge is to determine an optimal threshold for a given P_{FA}.

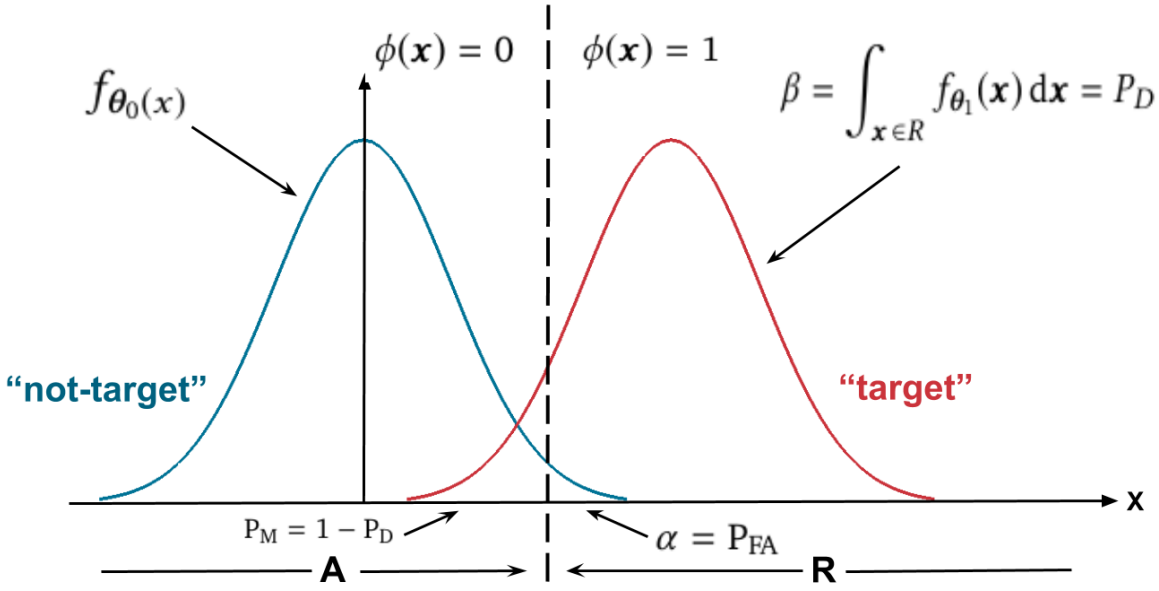

Figure 3.2: *Visual illustration of detection theory: The statistical distribution of "target" and "not-target" is shown. A threshold (dashed line) is set and the probability of false alarm, the probability of detection, and the probability of miss is defined. The different regions, A (acceptance) and R (rejection), corresponds to a data point being classified as "not-target" and "target" respectively (figure adapted from [21]).*

As can be seen in figure 3.2, P_D and P_{FA} are not independent of each other. In order to characterize the performance of a test, it is necessary to understand how P_D and P_{FA} behave together. The receiver operating characteristic curve (ROC), shown in figure 3.3, plots the two probabilities against each other, capturing

the relationship between them and describes the tradeoff between them for a given test [21]. In figure 3.3, the red dotted line corresponds to random guessing. The blue lines (A, B, and C) represent three different tests, where the test corresponding to line C performs better than the test corresponding to line B, which in turn performs better than the test corresponding to line A.

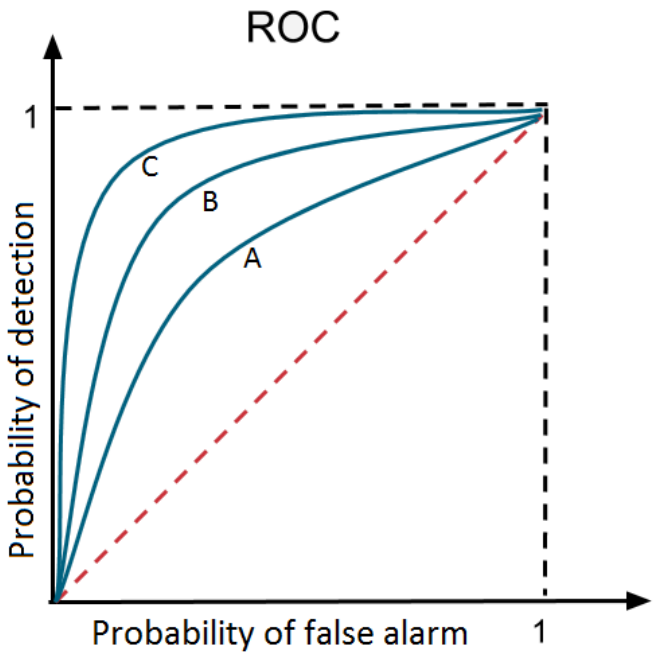

Figure 3.3: *Receiver operating characteristic (ROC) curve used for assessing the performance of a test, where P_D is plotted against P_{FA}. The red dotted line corresponds to a random guess, while the blue lines (A, B, and C) represent three different tests. The test corresponding to line C performs better than the test corresponding to line B, which in turn performs better than the test corresponding to line A (figure adapted from [21]).*

3.4 Statistical model for ocean clutter

The background is not uniform and will vary throughout the scene. Therefore, it is necessary to model the background sea clutter statistically and estimate the model parameters locally. One of the main challenges of ship detection is to find parametric distributions that can model the data accurately, without having a mathematical complex form and requiring complicated parameter estimators that lead to a heavy procssing load. For multiple target situations and situations involving heterogeneous ocean clutter, modelling the background will prove

especially challenging.

The simplest models for SAR amplitude and intensity are parameterized by the so-called equivalent number of looks (ENL) (to be presented in chapter 4.2.2) and the mean intensity. The ENL is an image constant which can be estimated prior to any detection process for a given set of SAR processing parameters [22]. The mean intensity must be estimated locally, and thus, an estimation sample is required. More advanced models, such as the K-distribution, requires additional local estimation of a shape parameter [7]. Therefore, for simplicity reasons, the scope of this thesis is restricted to the assumption of exponential distributed (single-look) and gamma distributed (multilook) data.

As mentioned in the previous paragraph, pixel values in a single look intensity image are assumed to follow an exponential distribution, while the pixel values in a multilook intensity image are assumed to follow a gamma distribution [23]. The following probability functions and cumulative distribution functions are given for the single-look case and the multilook case:

$$\text{Single-look:} \qquad p_X(x) = \frac{1}{\mu} e^{-x/\mu} \quad ; \quad x \geq 0 \tag{3.9}$$

$$\tag{3.10}$$

$$P_X(x) = 1 - e^{-x/\mu} \tag{3.11}$$

$$\tag{3.12}$$

$$\text{Multilook:} \qquad p_{X_L}(x) = \frac{1}{\Gamma(L)} \frac{L}{\mu} \left(\frac{Lx}{\mu} \right)^{L-1} e^{-Lx/\mu} \tag{3.13}$$

$$\tag{3.14}$$

$$P_{X_L}(x) = \frac{\gamma(L, Lx/\mu)}{\Gamma(L)} \tag{3.15}$$

where $\mu > 0$ is the mean value of each respective case, $\Gamma(\cdot)$ is the gamma function, $\gamma(\cdot, \cdot)$ is the lower incomplete gamma function, and L is the number of looks [1]. As mentioned in chapter 2.2, multilooking is a process that averages L single look measurements, where L is the number of looks. The fact that multilooked intensity data are gamma distributed is based on the assumption that the single looks are statistically independent. In reality, they are correlated. This means that the multilooked intensity data will not follow a gamma distribution with shape parameter L, and the actual distribution of the data is unknown. Thus, a reduced value of L, referred to as the equivalent number of looks (presented in chapter 4.2.2) is introduced. This value is assumed to be the same throughout the whole image and can be estimated from the data [22].

3.5 Algorithm: Constant false alarm rate (CFAR)

One of the reasons for using CFAR algorithms is that it is possible to model the ocean background. Optimal algorithms which minimizes P_D, such as the Neyman-Pearson detector, will require modeling of both the ocean background and targets. In our case, we have targets that vary too much to model. In order to model the statistical distribution of ships, an a priori knowledge is nedeed, such as the ship's size, its material, the orientation in relation to the radar's incidence angle, etc [17] [21].

As mentioned earlier, ships will appear as high intensity bright objects on an otherwise dark background. There are other objects in an ocean scene that, like a ship, have high intensity values. When these objects are classified as ships, a false positive decision is produced, and they are often referred to as false alarms. False alarms may occur due to, for example, ice bergs, oil rigs, breaking waves, or small islands. When $P_{FA} > 0$ for a given $f_{\boldsymbol{\theta}_0}(\boldsymbol{x})$, homogeneous ocean clutter will also cause false alarms. The constant false alarm algorithm is an adaptive thresholding algorithm based on a desire to ensure that the probability of false alarms (false alarm rate) is constant [17]. Because of the high intensity of the ship compared to the background, a threshold will be applied, where pixels with intensities above this threshold will be classified as ships, and pixels with values below this threshold will not. A threshold based on the P_{FA} can be determined from $f_{\boldsymbol{\theta}_0}(\boldsymbol{x})$ alone. The threshold will be set based on parameters such as the equivalent number of looks and mean intensity, as well as the desired false alarm rate [17].

Energy from the sidelobes might interfere with the estimation of sea clutter statistics, which is why a guard area is introduced. In figure 3.4, two possible ways of selecting the window for the estimation sample are illustrated. Energy from sidelobes will be avoided by choosing the estimation sample based on figure 3.4-a. By centering the estimation sample as in figure 3.4-b, data is selected closer to the pixel evaluated. The estimation sample size in figure 3.4-a and figure 3.4-b is the same size. The black square in the middle represents the pixel being evaluated, while the gray shaded area is the estimation sample [1].

The CFAR algorithms constitute a large family. The simplest algorithm is called the cell averaging CFAR(CA-CFAR) detector. By using the aforementioned guard area, potential sidelobes are discarded and the surrounding sea clutter is assumed to be homogeneous, meaning no targets are present [1]. The CA-CFAR algorithm computes the average intensity in each of the windows outside the guard area, which constitutes the estimation sample. Then, the mean intensity is computed by averaging each of the mean intensities from the windows. The threshold applied is based on the resulting mean intensity.

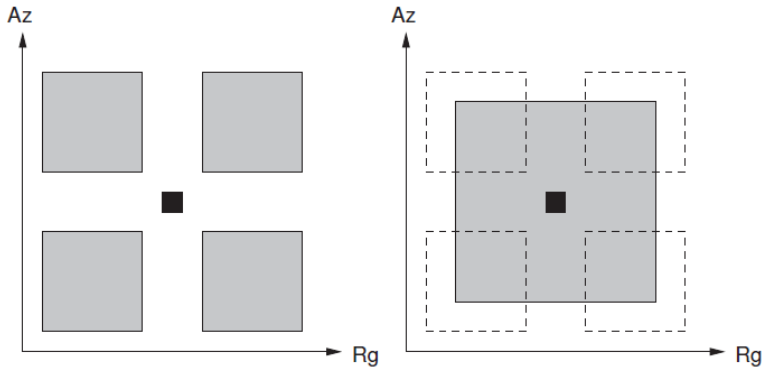

Figure 3.4: *Two possible ways of selecting the estimation sample(gray shaded area). The pixel being evaluated is the black square in the middle. Rg and Az represents range and azimuth direction, respectively (figure from [1]).*

Another CFAR algortihm is the greatest-of CFAR (GO-CFAR). The purpose of this algorithm is to handle heterogeneous sea clutter, specifically situations concerning edges. Instead of averaging the mean intensities from each of the corner estimation windows, the largest value is used to determine the threshold. In a lot of cases, especially close to the coast, the assumption of homogeneous sea clutter is violated. In big harbors, where there are multiple targets, some of these targets can be found inside the estimation sample, which will lead to an increase or overestimation of the applied threshold [19].

In situations where there are numerous ships present, detectors that handle estimation samples containing multiple targets may be used. The smallest-of CFAR (SO-CFAR) and order statistics CFAR (OS-CFAR) are examples of such detectors. The SO-CFAR calculates the mean intensity in each of the estimation windows, in which the lowest value is used as the sample estimate [1]. The OS-CFAR ranks the pixel values in the estimation sample by intensity and chooses a value with a certain rank as representative of the sample, to be used in threshold calculation [24].

Another tool that might be helpful when dealing with a scene where multiple targets exist, is iterative censoring. Iterative censoring can be applied to any of the other CFAR detectors and starts with defining an outlier map. Pixels that are indicated as outliers are censored out from the estimation sample before parameter estimation, threshold computation, and hypothesis testing is reiterated. When the outlier map stabilizes, the algorithm has converged. Although the iterative censoring algorithm generates good results, the iterations have a relatively high computational cost. The outliers that are removed from the estimation sample, will contain both actual targets and false alarms. It is

not possible to discriminate ships from false alarms, which is why statistics based on the estimation sample obtained from the iterative censoring scheme may be biased towards a value that is too low [1][25].

Concerning ship detection algorithms, it is of desire to develop algorithms that are fast, accurate, and that can handle scenarios with multiple targets as well as an inhomogeneous background. Tao et al. [1] propose a new ship detection algorithm based on truncated statistics. Because the number of censored points are known, while the number of data points representing ocean is unknown, the remaining sample can be regarded as truncated and handled according to the theory of truncated statistics [1]. The Cambridge dictionary of statistics [26] defines truncated data as data for which sample values larger (right truncated) or smaller (left truncated) than a specified value are not observed. Next, the goal is to find a way of computing the estimated mean of the truncated data.

The right-truncated version of the original estimation samle X, is denoted as $\widetilde{X}$. After a threshold t is applied to X, the probability density function (pdf) of $\widetilde{X}$ can be defined as

$$p_{\widetilde{X}}(x;t) = p_X(x|X < t) = \frac{p_X(x)}{P_X(t)} \tag{3.16}$$

where $p_X(x)$ and $P_X(t)$ is the pdf of X and cumulative distribution function (cdf) of X, repsectively. The parameter t is a user specified value called the truncation depth and should be set so that all possible targets are excluded [1].

The previous section introduced assumptions about the statistical distribution of single-look and multilook data. Single-look data is assumed to follow an exponential distribution, while mulitlook data is assumed to follow a gamma distribution. Their respective pdfs and cdfs were also defined. Thus, the truncated pdfs of the single-look and multilook intensity data, based on the estimation sample being right truncated with a truncation depth t, are given as [1]

$$\text{Single-look:} \qquad p_{\widetilde{X}}(x;t) = \frac{1}{\mu}\frac{e^{-x/\mu}}{1-e^{-t/\mu}} \quad ; \quad 0 \leq x < t \tag{3.17}$$

$$\tag{3.18}$$

$$\text{Multilook:} \qquad p_{\widetilde{X}_L}(x) = \frac{1}{\gamma(L, Lt/\mu)}\frac{L}{\mu}\left(\frac{Lx}{\mu}\right)^{L-1} \tag{3.19}$$

In Tao et al. [27], an estimator for the mean value was found for both the truncated single-look intensity image and the truncated multilook intensity image. Both estimators are maximum likelihood estimators that need to be

solved numerically

$$\text{Single-look:} \qquad \hat{\mu} = \frac{1}{n}\sum_{i=1}^{n} x_i + \frac{t}{e^{t/\hat{\mu}} - 1} \tag{3.20}$$

$$\text{Multilook:} \qquad \{\hat{\mu}\} \subseteq \{\arg\max_{\mu} \mathscr{L}(\mu|x)\} \tag{3.21}$$

The log-likelihood function is defined as

$$\log \mathscr{L}(\mu|x) = nL \log \frac{L}{\mu} - n \log \gamma(L, tL/\mu) - \frac{nL}{\mu}\frac{1}{n}\sum_{i=1}^{n} x_i + n(L-1)\frac{1}{n}\sum_{i=1}^{n} \log(x_i) \tag{3.22}$$

where $\{x_i\}_{i=1}^{n}$ is a sample of size n, t is the truncation depth, L is the equivalent number of looks, and $\gamma(\cdot,\cdot)$ is the lower incomplete gamma function [27].

Tao et al. [27] tested the truncated statistics CFAR (TS-CFAR) against CA-CFAR and OS-CFAR, both with and without the implementation of the iterative censoring (IC) scheme (ICCA-CFAR, ICOS-CFAR). The CA-CFAR is one of the most commonly used CFAR algorithms and the OS-CFAR is known as a state of the art CFAR algorithm, especially when implemented with an iterative censoring scheme. They found that the TS-CFAR is superior to the CA-CFAR and OS-CFAR, and it performs as well as the IC scheme algortihms. Also it regulates the false alarm rate extremely well, that is a constant false alarm rate is maintained throughout the scene. Another advantage of using a TS-CFAR algorithm is that there is no need for guard areas, since sidelobes will be removed in the truncation process.

This CFAR algorithm serves as an inspiration for the idea of this project. In order to find the best possible estimate for the radar cross section of the ocean, speckle has to be removed. By applying a low pass filter in the frequency domain, the process of suppressing speckle will be fast. However, by removing high frequecies, high intensity target pixels and other artefacts will be smeared out in the spatial domain after reconstruction. Therefore, a threshold in the spatial domain will have to be applied to the dataset first, in order to truncate the data. This will result in an irregular grid, which promts the use of the non-uniform fast Fourier transform. This process will be described further in the following chapters.

4

Methods

A new algorithm for estimating the underlying ocean reflectivity is proposed in this project. The output of the propsed algorithm will be an estimation of the ocean radar cross section, and a threshold can be calculated based on this output. The resulting threshold will serve as an input to a ship detection algorithm, such as a CFAR algorithm. The proposed algorithm is inspired by one of the algorithms described in section 3.5, specifically, the ship detection algorithm based on truncated statistics. The idea is to speckle filter the data by lowpass filtering in the frequency domain, yielding a fast process. Lowpass filtering in the frequency domain is a non-adaptive filter and will therefore smear edges and point targets. However, it is assumed that a natural ocean surface is sufficiently smooth for the non-adaptive lowpass filter not to introduce critical distortions of the image, and that the speed of the proposed algorithm will outweigh the drawbacks of the simplistic approach. To enforce the required smoothness, truncation of high intensity pixels is used to remove targets and related artifacts.

Speckle filtering the SAR image will produce an image of pixel-level estimates of the underlying radar reflectivity. A threshold for a simple CFAR detector can be set based on these, where the intensity values are assumed to be gamma distributed. This thresholding operation is complicated by the presence of targets. These targets might be accompanied by artefacts such as ghosts and sidelobes, whose energy will be smeared out in the spatial domain after reconstruction. Therefore, it is proposed to remove these targets before transforming the image into the frequency domain. That is, a fraction of the highest intensity pixels

will be truncated prior to the frequency domain tranformation.

Problems arise after some of the image pixels have been removed, because the truncated image forms an irregular grid. The idea is to use a fast Fourier transform (FFT) to transform the image to the frequency domain, but because the truncated image is an irregular grid, a traditional FFT cannot be applied. The FFT algorithm requires the input data to be sampled uniformly [28], which is not the case for the truncated SAR image. It is predicted that the problem can be solved by using a special version of the FFT, called the non-uniform or non-equispaced FFT, often referred to as NFFT or NUFFT.

Figure 4.1 summarizes the different steps in the proposed algorithm for fast estimation of the underlying radar reflectivity and this chapter will deal with the different methods needed to execute the new algorithm. The prediction is that the combination of truncation and thresholding will proivde a fast algorithm that can handle cases where multiple targets are present, as well as clutter edge (nonstationary clutter) cases, thus yielding a flexible and efficient algorithm.

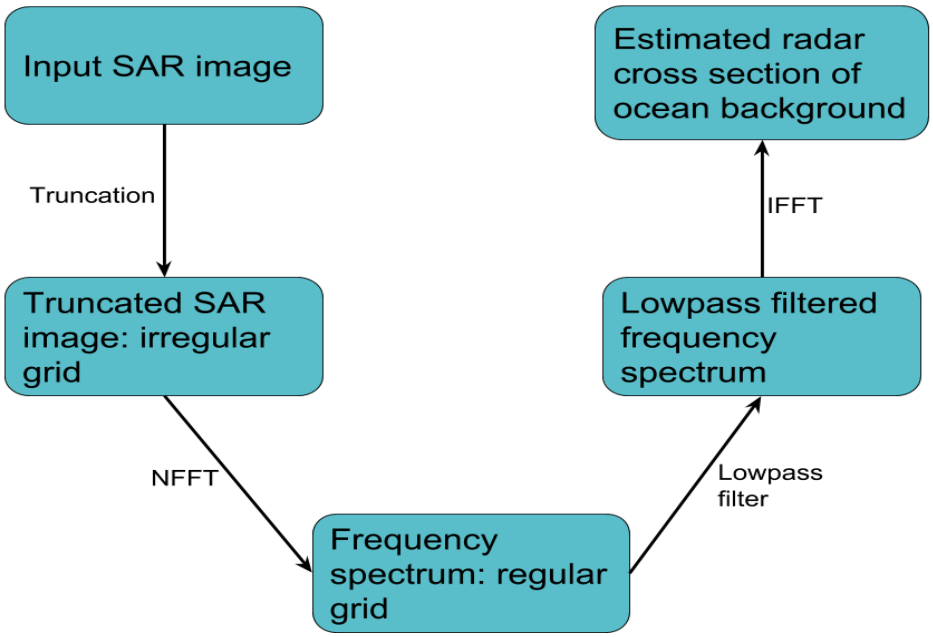

Figure 4.1: *Outline of proposed algorithm.*

4.1 Lowpass filter

A lowpass filter attenuates high frequencies, while passing low frequencies and applying a lowpass filter to an image will result in a blurred image. A lowpass filter can be applied in both frequency and spatial domain. A major advantage of using a frequency based filter instead of a spatial filter, is computation time. A frequency filter will be computationally faster then the spatial filter. Because one of the goals of this thesis is to construct a fast algorithm, a frequency filter will be implemented. For this project, three lowpass filters were evaluated: an ideal lowpass filter (ILPF), a Butterworth lowpass filter (BLPF), and a Gaussian lowpass filter (GLPF). These three filters are fairly simple and depend on few parameters, as opposed to other lowpass filters such as Chebyshev filters and the elliptic filter. Another possibility is to perform lowpass filtering by using window functions. Because the goal is to preserve as much as possible of the signal, while attenuating high frequencies due to speckle, this option is also discarded [29].

An ILPF has a sharp cut-off frequency and therefore produces a ringing effect which can be seen in the filtered image. This is an undesireable effect, which is why the ILPF was discarded. The GLPF has sufficient smoothing abilities, while avoiding ringing effects, but the BLPF was chosen for this projoct. The BLPF is an order-based filter (see figure 4.2), where a low order BLPF will approach a GLPF and a high order will approach an ILPF. The BLPF will provide tighter control of the transition between low and high frequencies about the cutoff frequency compared to the GLPF. The BLPF with order $n = 2$ was implemented, which is a tradeoff between effective filtering and acceptable ringing [29].

The transfer function of the BLPF of order n and with cutoff frequency at a distance D_0 from the origin is defined as follows [29]

$$H(u,v) = \frac{1}{1 + [D(u,v)/D_0]^{2n}} \tag{4.1}$$

where $D(u,v)$ is defined as

$$D(u,v) = \left[(u - P/2)^2 + (v - Q/2)^2\right]^{1/2}. \tag{4.2}$$

P and Q are the dimensions (i.e. size) of the filter, while u and v are discrete frequency variables.

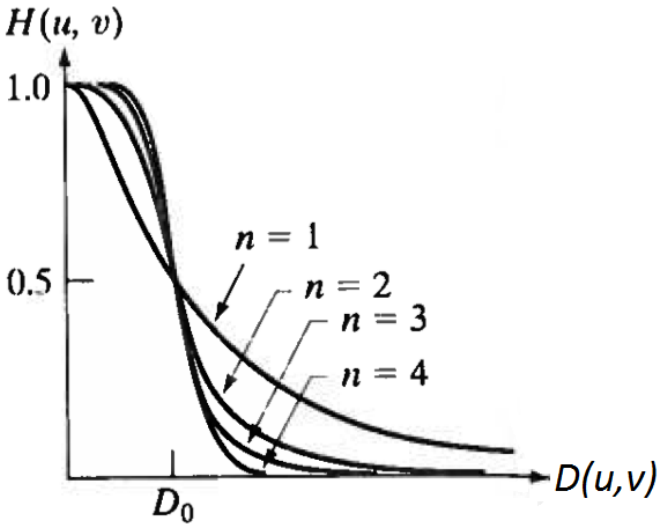

Figure 4.2: *The Butterworth lowpass filter is an order based filter and the figure illustrates various orders and its effect. A low order will approach a GLPF, while a high order will approach an ILPF (figure from [29]).*

4.2 Frequency Threshold

The newly proposed algorithm will require lowpass filtering in the frequency domain. The goal of the lowpass filtering is to suppress speckle that is present in the image. Removing speckle will result in a blurred image with edges and similar features smeared out. The algorithm is meant to be tested on Radarsat-2 data (to be presented in chapter 5.3), and a majority of the SAR images present in the dataset will contain features that have to be preserved. Examples of such features are raincells, wind shadows, and imprints of low pressures. This indicates that multiple criteria is necessary in order to determine the frequency threshold [14].

Suppressing speckle from an image is equivalent to removing the high frequencies, while preserving edges require preservation of the high frequencies [30]. In order to evaluate the effect of the lowpass filter and determine a suitable threshold, simulated data are needed. Therefore, three gradient images have been acquired (to be presented in chapter 5.2). The Radarsat-2 data used for ship detection purposes are commonly multilook intensity products, also known as detected products. These data are often modeled with the gamma distribution, which can be derived as the theoretical distribution under the assumption of fully developed speckle and constant radar cross section. Therefore, randomly distributed gamma data was simulated and multiplied with

each of the gradient images that simulate a nonstationary ocean background. The resulting speckled images will be used to study the impact of the frequency threshold.

The goal is to find a threshold which produces the right compromise between speckle suppression and preservation of details, such as edges and other important features. Hence, four different measures are introduced:

- Speckle Suppression Index (SSI)
- Equivalent Number of Looks (ENL)
- Edge Preservation Index (EPI)
- Sum of Squared Error (SSE)

ENL and SSI are measures related to speckle strength and smoothing, while the EPI is a measure related to preservation of edges and other features in the images. Smoothing and detail preservation are conflicting criteria that must be balanced to detemine the frequency threshold. The SSE will provide a measure of the overall deviation of the filtered image from the original image.

4.2.1 SSI

The Speckle Suppression Index (SSI) is widely used in the literature and is commonly used for evaluating various speckle filters [31][14][32]. The SSI is used to measure speckle strength in an image and is defined as

$$\mathrm{SSI} = \frac{\sqrt{\mathrm{var}(I_f)}}{\mathrm{mean}(I_f)} \frac{\mathrm{mean}(I)}{\sqrt{\mathrm{var}(I)}} \tag{4.3}$$

where I is the intensity of the original speckled image and I_f is the intensity of the filtered image.

The filtered image will contain less speckle and will therefore tend to have a diminished variance. A number of different sources in the literature claims that the SSI value will generally be less than one, which will be verified in chapter 6.1. Also, the smaller the value is, the greater the speckle suppression [31].

4.2.2 ENL

As mentioned earlier, the final algorithm will be tested on multilook intensity images (MLI). Multilook intensity images are assumed to follow a gamma distribution with mean (scale parameter) σ and order (shape) parameter L [7]

$$p_I(I;\sigma,L) = \frac{1}{\Gamma(L)}\left(\frac{L}{\sigma}\right)^L I^{L-1}e^{-LI/\sigma} \qquad I \geq 0 \tag{4.4}$$

The images are produced by averaging L single look measurement. The assumption that the multilook intensity images follow a gamma distribution with shape parameter L is based on the assumtion of uncorrelated single look measurements. Because the single look measurements are in fact correlated, a new parameter is introduced. This new parameter is the Equivalent Number of Looks and one way to estimate it is [22]

$$\text{ENL} = \frac{\text{mean}(I_f)^2}{\text{var}(I_f)} \tag{4.5}$$

where I_f is the filtered image. Because the single look measurements are not statistically independent, the actual distribution of the data is not known. This is solved by replacing the actual number of looks with the ENL as a shape parameter in the gamma distribution. Thus, with the help of the ENL, the gamma distribution will fit the data [22].

Similarly to the SSI, the ENL measures speckle strength or degree of smoothing over a homogeneous region in an image. A higher value for the ENL indicates a higher level of averaging and thus greater speckle suppression [33]. A variety of different estimators for the ENL has been derived [22], but for the purpose of using the ENL to determine a frequency threshold, the traditional ENL (equation 4.5) estimator was used. If the thesis is successful in developing a complete algorithm and Radarsat-2 data are to be utilized, a state of the art ENL estimator developed by Anfinsen et al. [22] is meant be used.

4.2.3 EPI

The ENL and the SSI are both indices that provide information about speckle strength in an image. As mentioned in chapter 4.2, a lot of the SAR images in the Radarsat-2 dataset will contain a variety of features. Therefore, some kind of edge preservation index is needed. In the literature, several different measures are suggested to evaluate a filter's ability to preserve/retain edges [34][35][14][32]. They are all designed in a similar way and seem to be based on the same idea. For the purpose of the task at hand, the following Edge

Preservation Index was implemented [34]

$$\text{EPI} = \frac{\sum |I_f(i,j) - I_f(i-1,j+1)|}{\sum |I(i,j) - I(i-1,j+1)|} \tag{4.6}$$

where $I(i,j)$ is the intensity value of a detected edge pixel and $I_f(i,j)$ is its corresponding intensity value in the filtered image. As can be seen from how the equation is set up, the result of this equation is not independent of direction. Some of the other EPI's that exist are defined such that it measures the EPI in a specific direction, such as horizontal or vertical EPI's [35]. Implementing these instead of equation (4.6), yielded the same results. Defining a neighborhood around the pixel being evaluated and replacing the mean of this neighborhood with $I_f(i-1,j+1)$ and $I(i-1,j+1)$ in equation (4.6) also yielded the same result. Therefore, the equation that was easiest to implement was chosen, i.e. equation (4.6). Some of the literature claims that this index should be in the range $[0,1]$, where a higher value corresponds to a better preservation of edges [34][36]. From implementing and testing on the three gradient images to be presented, it appears that this may not be the case here.

Canny edge detection

The EPI cannot be computed before edge pixels have been detected. This is done by implementing a Canny edge detection algorithm. The algorithm was developed by John F. Canny in 1986 and is based on three performance critera [37]:

- Good detection: no edges should go undetected and there should be no response where an edge does not exist.
- Good localization: the distance between a pixel classified as an edge pixel and the actual edge pixels should be as small as possible.
- Only one response to a single edge: if an edge pixel has two detected edges corresponding to it, one of them has to be considered erroneous.

It consists of the following steps [29]:

1. Before edges can be detected, noise in the image has to be filtered out. This is achieved by applying a Gaussian filter.
2. The edge strength is found by computing the gradient magnitude.
3. Find the edge direction by computing angle images.

4. Apply nonmaxima suppression to the gradient magnitude image. This will eliminate false responses detected by previous steps.

5. Double thresholding and connectivity is applied to detect and link edges.

Edge detection algorithms that are especially designed for handling SAR images or images that contain speckle will probably yield better results [38][39][23][40].

4.3 SSE

The SSE is a purely obejective error measurement which will bear in mind both detail preservation and smoothing in its calculation. It compares, pixel by pixel, a filtered image with the corresponding noise-free/clean image. Therefore, because the SSE requires a clean image, it is not possible to use the error measure operationally. The SSE is defined as [41]

$$SSE = \sum \left(I(i,j) - I_f(i,j)\right)^2 \tag{4.7}$$

where I is the intensity of the original speckled image and I_f is the intensity of the filtered image.

4.4 Fourier Transform

The key idea is to utillize the FFT to achieve high processing speed, while handling the cases of heterogeneous ocean background and multiple targets simultaneously.

Any given signal can be expressed as the sum of sines and/or cosines of different frequencies, where each of these sines and cosines are multiplied with different coefficients. Based on this, the one-dimensional continuous Fourier transform and its inverse is defined as follows [29]

$$\text{FT}: \quad F(\mu) = \int_{-\infty}^{\infty} f(t) e^{-j2\pi\mu t}\, \mathrm{d}t \tag{4.8}$$

$$\updownarrow \tag{4.9}$$

$$\text{IFT}: \quad f(t) = \int_{-\infty}^{\infty} F(\mu) e^{j2\pi\mu t}\, \mathrm{d}\mu \tag{4.10}$$

Similarly, the two-dimensional continuous Fourier transform (FT) and its in-

verse (IFT) is defined as follows [29]

$$\text{FT}: \quad F(\mu, v) = \int_{-\infty}^{\infty} \int_{-\infty}^{\infty} f(t, z) e^{-j2\pi(\mu t + v t)} \, \mathrm{d}t \tag{4.11}$$

$$\updownarrow \tag{4.12}$$

$$\text{IFT}: \quad f(t, z) = \int_{-\infty}^{\infty} \int_{-\infty}^{\infty} F(\mu, v) e^{j2\pi(\mu t + v t)} \, \mathrm{d}v \tag{4.13}$$

where $f(t)$ is a continuous function of a continuous variable t and $f(t, z)$ is a continuous function of continuous variables t and z in the time/spatial domain. $F(\mu)$ is also a continuous function of a continuous variable μ and for the two-dimensional case, $F(\mu, v)$ is a continuous function of continuous variables μ and v in the frequency domain. The fast Fourier transform is essentially a mapping from the time/spatial domain to the frequency domain or vice versa, in which all information is preserved.

An important and extremely useful property of the Fourier transform is the convolution theorem [29], which states that a convolution in the spatial domain is equivalent to a multiplication in the frequency domain, and vice versa. It can be expressed in the following manner

$$f(t) \star h(t) \Leftrightarrow H(\mu) F(\mu) \tag{4.14}$$

$$\updownarrow \tag{4.15}$$

$$f(t) h(t) \Leftrightarrow H(\mu) \star F(\mu) \tag{4.16}$$

where $f(t)$ and $h(t)$ are two continuous functions of continuous variable t in the spatial domain and $F(\mu)$ and $H(\mu)$ are two continuous functions of continuous variable μ in the frequency domain. When performing filtering in the spatial domain, convolution is often utilized, which can be extremely time consuming. Therefore, as multiplication is much faster, the convoution theorem is an extremly powerful tool of the Fourier transform.

In real life, all recorded signals are sampled with a finite number of samples. In order to completely recover a bandlimited function from its samples, the sampling theorem must be kept in mind. The sampling theorem states that a bandlimited function can be completely recovered by applying a sampling rate that exceeds twice the highest frequency content of the given function. A bandlimited function is a function, in which its Fourier transform is zero for frequencies outside a finite interval. Thus, a discrete Fourier transform that corresponds to the real life situation is needed. The two-dimensional discrete Fourier transform (DFT) and its inverse (IDFT) is described as follows

[29]

$$\text{DFT}: \quad F(u,v) = \sum_{x=0}^{M-1}\sum_{y=0}^{N-1} f(x,y)e^{-j2\pi(ux/M+vy/N)} \tag{4.17}$$

$$\updownarrow \tag{4.18}$$

$$\text{IDFT}: \quad f(x,y) = \frac{1}{MN}\sum_{u=0}^{M-1}\sum_{v=0}^{N-1} F(u,v)e^{j2\pi(ux/M+vy/N)} \tag{4.19}$$

$$\tag{4.20}$$

where $f(x,y)$ is an image of size $M \times N$, and $F(u,v)$ is its transform. Variables x and y are discrete coordinates in the spatial image, while u and v are frequency variables. When working with SAR images in MATLAB, a frequency representation is obtained by using the MATLAB function *fft2*. This function computes the two-dimensional discrete Fourier transform with a two-dimensional fast Fourier transform algorithm [42]. This allows the approximation of the Fourier transform computation to be fast and with few arithmetic operations.

One limitation of the FFT that has to be adressed, is its disability when it comes to handling unequally spaced samples [43]. Truncating a SAR image to remove high-intensity pixels will result in an irregularly spaced grid, and therefore the FFT cannot be used to transform the data to the frequency domain. Thus, the nonequispaced fast Fourier transform is introduced.

4.4.1 Nonequispaced Fast Fourier Transform (NFFT)

The nonuniform FFT (NFFT) is used in a number of different areas. Some examples of applications include synthetic aperture radar, medical imaging, telecommunications, geoscience, and seismic analysis [44]. For remote sensing, the NFFT has mostly been used in SAR focusing algorithms, such as the $\omega - k$ algorithm [45]. For the sake of simplicity, this section will start off with the theory of the one-dimensional NFFT before extending the theory to D dimensions. A detailed analysis of the nonuniform FFT is outside the scope of this thesis, and the main focus will be on introducing the NFFT, applying it to real truncated SAR data, and evaluating its performance in relation to the task at hand.

Several papers and articles have been written concerning the NFFT and some authors have developed MATLAB and/or C programming interfaces for carrying out the calculation. Two of the most known interfaces were developed by Keiner et al. and Fessler et al. The software developed by the former is primarily a C software library, while the software developed by Fessler et al. consists of MATLAB code [46] [47] [48]. Most of the literature concerning the calculation

of the NFFT is based on utilizing a window function and applying a FFT to an oversampled grid [49]. The purpose of the NFFT in this thesis is to transform an irregular grid in the spatial domain to the frequency domain where it can be lowpass filtered, and thus being able to perform a fast speckle reduction.

With the current situation in mind, there are three main steps to calculating the NFFT for a given one-dimensional signal and they can be summed up as follows [46][50]:

1. Convolve the original nonuniformly sampled signal with a one-dimensional, 1-periodic window function

2. Compute the standard fast Fourier transform on an oversampled grid

3. Deconvolution to correct for the convolution in step one

A 1-periodic function is a function that has no other periods than $\pm\omega, \pm 2\omega, \pm 3\omega, \ldots,$. The three steps mentioned above are sometimes referred to as gridding, type-1 NUFFT, or the transposed version of the NFFT [51] [50] [52]. Next, the three main steps in the NFFT algorithm will be mathematically reviewed.

4.4.2 One-dimension

The goal of the one dimensional NFFT is to compute [52]

$$F(u) = \sum_{k=1}^{M} f_k e^{-j2\pi u x_k / M} \tag{4.21}$$

at given nonequispaced nodes x_k, where $u = -M/2, \ldots, M/2 - 1$. This computation is to be executed fast.

Parameters $\alpha > 1$ and $n = \alpha M$ are defined as the oversampling factor and FFT length, respectively. It is important that the window function is well localized in both the frequency domain and the spatial domain. The input domain is referred to as the spatial domain, since the transform will be applied to images, although it can in principle also be a time domain. A window function φ and its Fourier series $\tilde{\varphi}$ is given. By truncating the Fourier series $\tilde{\varphi}$ at length n, a window well localized in the frequency domain is obtained. Truncating the Fourier series at length n will give rise to an aliasing error. By truncating the window function φ with a cut-off parameter $m << n$, a window well localized in the spatial domain is obtained. Truncating the window function with cut-off parameter m will give rise to a truncation error [49]. The window well localized in the frequency domain is referred to as D, while the window well localized

in the spatial domain is referred to as ψ.

Step 1

The first step is to convolve the nonuniformly sampled signal with a one dimensional, 1-periodic, continuous window function ψ, that is well localized in the spatial domain. Thus, for $l = -n/2, \ldots, n/2-1$, the first step is executed by [52]

$$G_l = \sum_{k=1}^{M} f_k \psi \left(x_k - \frac{l}{n} \right) \tag{4.22}$$

Step 2

Step two of the NFFT is to oversample the result from step one and apply a standard FFT. Thus, for $u = -M/2, \ldots, M/2 - 1$, step two is executed by [52]

$$\widehat{G}_u = \frac{1}{n} \sum_{l=-n/2}^{n/2-1} G_l e^{-j2\pi ul/n} \tag{4.23}$$

Step 3

Once the FFT has been computed, the last step will be a deconvolution of the result from the previous step with a window function that is well localized in the frequency domain. Thus, for $u = -M/2, \ldots, M/2 - 1$, the third step is executed by [52]

$$F(u) \approx S(u) = \frac{\widehat{G}_u}{D(u)} \tag{4.24}$$

where $D(u)$ is the frequency representation of the window function, i.e.

$$D(u) = \int_{-l/2}^{l/2} \tilde{\varphi}(x) e^{-j2\pi ux} \, \mathrm{d}x \tag{4.25}$$

and $S(u)$ is an approximation of $F(u)$. Naturally, it is desirable for the approximation error to be as small as possible.

As previously mentioned, the window function should be well localized in both time/spatial and frequency domain. It is important to use a window function in which the truncation error and the aliasing error is minimized [53]. Several window functions have been proposed and evaluated in regards to

their characteristics and the error they cause. Some of the different windows proposed are [51] [46]:

- Gaussian
- Gauss pulse tapered with a Hanning window
- B - splines
- Sinc functions
- Kaiser-Bessel functions
- Numerically optimized filter that minimizes the relative maximum absolute error and the root mean square error

Depending on the available memory, it is proposed to precompute the window function before executing the NFFT algorithm, which will result in a fast procedure. Therefore, the choice of window function will depend on the required accuracy and memory needed for the precomputation [53].

4.4.3 D > 1 dimensions

For D dimensions greater than one, the multivariate window function is defined as [53]

$$\varphi(\boldsymbol{x}) = \varphi_0(x_0)\,\varphi_1(x_1)\ldots\varphi_{D-1}(x_{D-1}) \tag{4.26}$$

where $\varphi_0, \ldots, \varphi_{D-1}$ are univariate window functions and $\boldsymbol{x}$ is a node represented by $\boldsymbol{x} = (x_0, \ldots, x_{D-1})^T$. A multivariate window function well localized in the spatial domain and frequency domain is approximated from the multivariate function φ and its Fourier series $\tilde{\varphi}$, respectively. Besides having to utilize a D-dimensional FFT in the second step, the algorithm is otherwise the same for all D dimensions.

The majority of the literature uses the same procedure as the one just described. Greengard and Lee proposed a way to accelerate the nonuniform FFT without precomputation. They wished to improve the computation time of step two with a procedure called fast Gaussian gridding, which they claim will have particular value for the two and three-dimensional case [50]. Fessler and Sutton proposed the use of min-max interpolation in order to obtain a higher accuracy. They found, through numerical results, that their proposed interpolation method provided lower approximation errors compared to conventional interpolation methods [47]. Because the goal of this thesis is to develop a

fast algorithm and the fact that an inaccurate, non-adaptive speckle filter has already been chosen, applying Fessler and Sutton's min-max interpolation will prove unnecessary.

To summarize, a schematic illustration of the one dimensional NFFT algorithm is illustrated in figure 4.3. The oversampling factor in the figure is set to $\alpha = 2$ (i.e. $n = 2M$). The figure goes through the steps from convolution and oversampling in time/spatial domain to applying a FFT and deconvolution in the frequency domain.

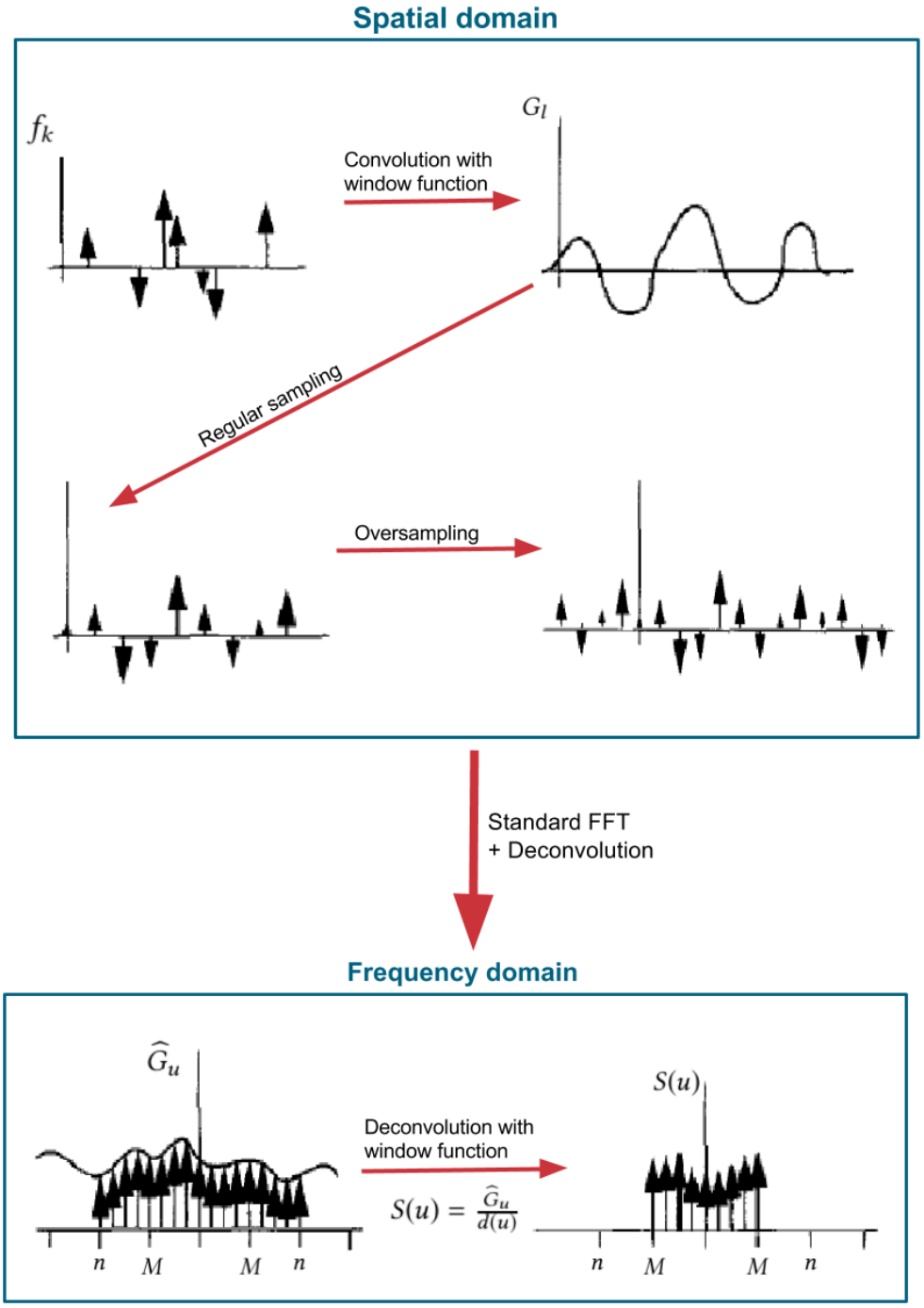

Figure 4.3: *Schematic overview of the one-dimensional NFFT algorithm from convolution and oversampling in spatial domain to applying a FFT and deconvolution in frequency domain. The oversampling factor is set to $\alpha = 2$, i.e. $n = 2M$ (figure adapted from [51])*

5 Data

The data that is ment to be used in this project consists of two datasets. The first dataset contains three gradient images, while the second dataset contains Radarsat-2 images. In the following sections, the two datasets and the Radarsat-2 satellite will be presented.

5.1 Radarsat-2

RADARSAT-2 was launched on December 14th, 2007, from Russia's Baikonur Cosmodrome in Kazakhstan. It is a cooperation between the Canadian Space Agency (CSA) and MacDonald Dettwiler Associates Ltd. (MDA). It is a SAR satellite (operates day and night in all weather conditions) that operates in the C-band at a frequency of 5.405 GHz. It follows a sun-synchronous polar orbit with a mean altitude of 798 km and an orbital period of approximately 101 minutes. It does about 14 orbits per day and has a repeat cycle of 24 days [54].

RADARSAT-2 has a variety of improvements compared to its predecessor (RADARSAT-1). It has a greater flexibility in regards to its polarization (offers quadrature polarization), higher resolution, left and right looking imaging options (which leads to shorter revisit time), larger data storage, and shortened programming, processing, and delivery timelines [55]. Also, it has a Global Positioning System (GPS) onboard, which allows for increased geometric accuracy

[55]. Its minimum timeline is 7 years, which means that it is currently in its 7th year of operation. Reports from july 2014 state that the satellite continuous to perform well and that system performance targets continue to be met or better [54]. Therefore, like its predecessor, it is likely that this satellite will be operational for quite a few more years to come.

RADARSAT-2 offers single, dual, and fully/quadrature polarimetric imaging modes with spatial resolutions ranging from 3 m in the Ultra-fine mode to 100 m in the ScanSAR Wide mode. Its swath widths vary from 18 km to 500 km. An overview of the different modes offered can be seen in figure 5.1. For the purpose of this project, it is worth mentioning that the Ultra-Fine mode with a resolution of 3 m, will improve ship detection and offers potential for ship classification [56]. Although, using this mode will make it impossible to monitor larger areas, which is desirable in ship detection. Therefore, a mode that provides a larger swath width should be utilized.

The key priorities of the RADARSAT-2 mission is to respond to the challanges of monitoring the environment, managing natural resources, and performing coastal surveillance. Thus, the satellite provides information related to for example ice monitoring, disaster management, detection of structural differences in forests, crop mapping, mapping of fine geological structures, oil spill monitoring, and ship detection.

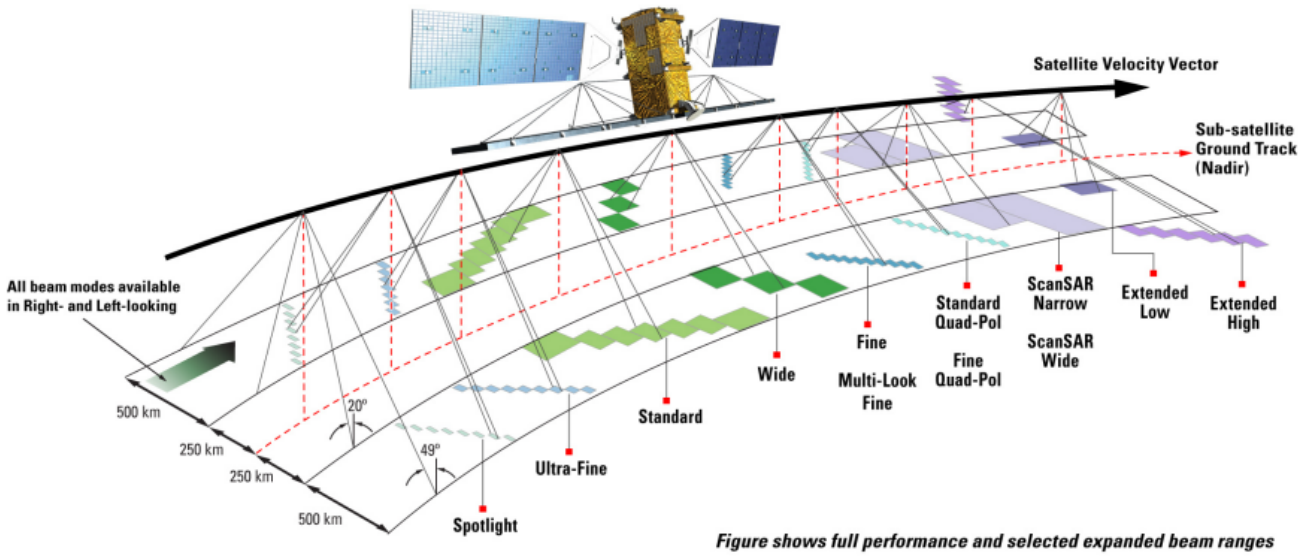

Figure 5.1: *RADARSAT-2 SAR modes of operation (figure from [57]).*

5.2 Dataset 1: Gradient Images

The first dataset contains simulated data and will be used for determining the threshold of the lowpass filter that will later be applied in order to suppress speckle in a SAR image. As will be explained in the following section, dataset 2 consists of multilooked Radarsat-2 images and will therefore contain intensity gamma distributed speckle. Therefore, simulated speckle was multiplied with each of the gradients. The three gradient images are presented in figure 5.2, figure 5.3, and figure 5.4 both with and without speckle. The speckled gradient images were simulated multiple times with uncorrelated speckle, such that ENL= L. The images were simluted with L ranging from $L = 2$ to $L = 16$. However, because the real SAR data that is meant to be used in this thesis has nominal number of looks equal to either four or eight, the speckled gradient images were simulated with shape parameter $L = 4$.

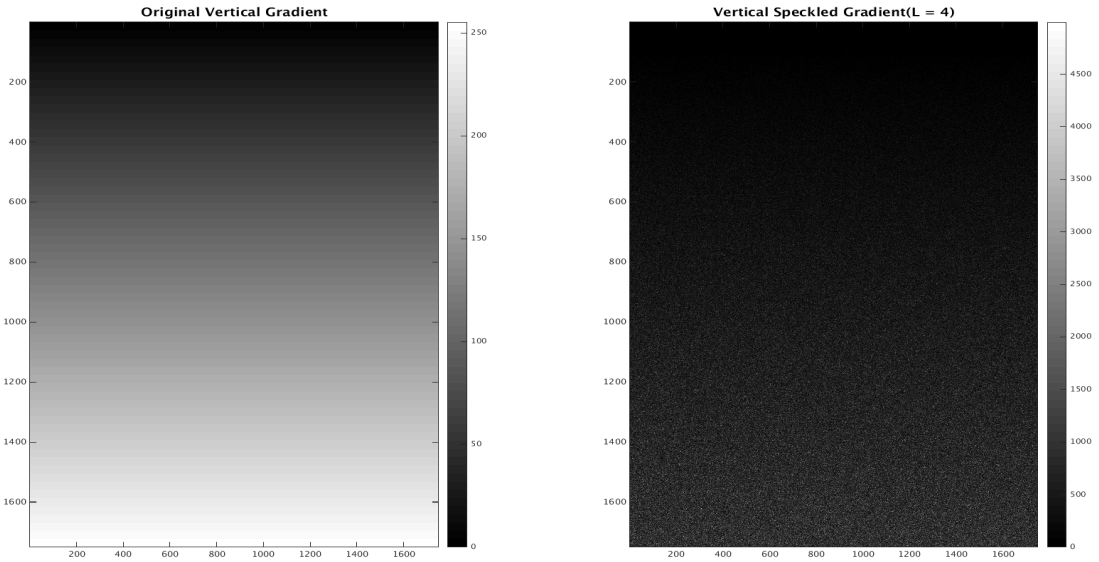

Figure 5.2: *Original vertical gradient with and without speckle. Speckle simulated with shape parameter $L = 4$.*

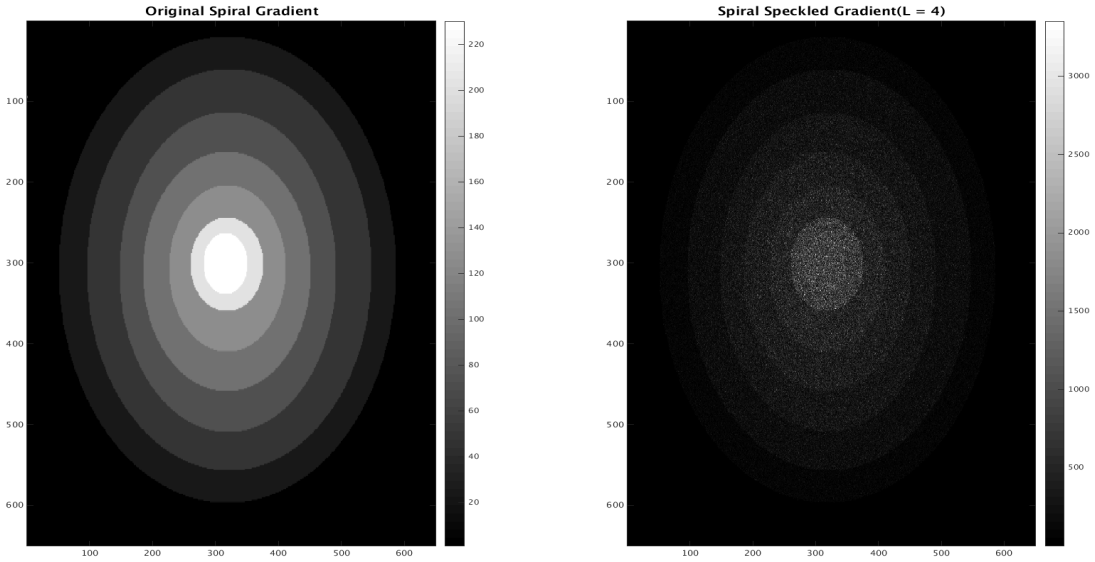

Figure 5.3: *Original spiral gradient with and without speckle. Speckle simulated with shape parameter $L = 4$.*

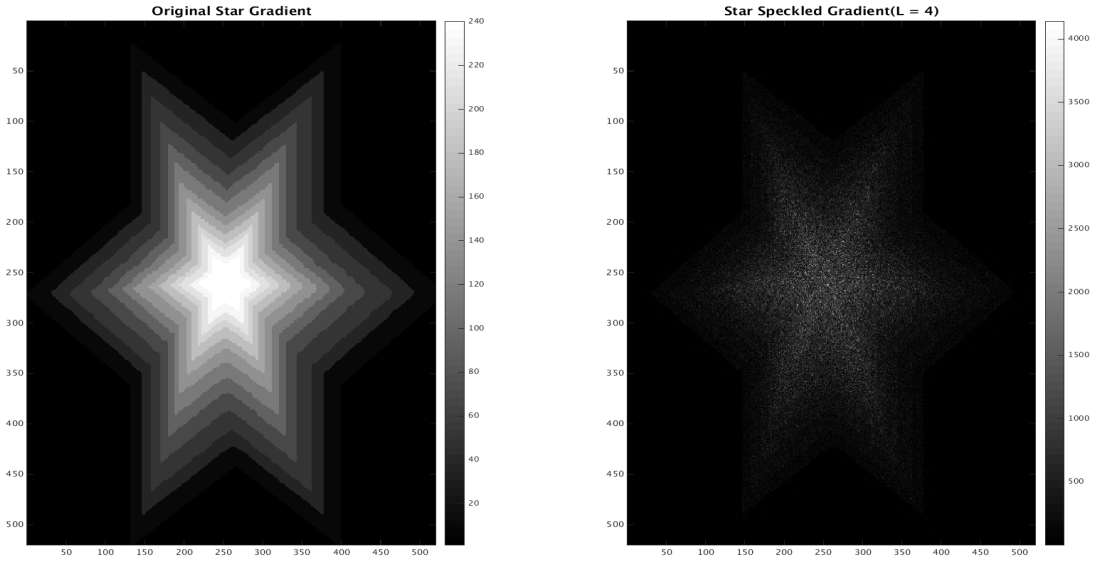

Figure 5.4: *Original star gradient with and without speckle. Specke simulated with shape parameter $L = 4$.*

5.3 Dataset 2: Radarsat-2

The second dataset contains detected Radarsat-2 SAR images acquired by Kongsberg Spacetec AS (KSPT). All of the images have been multilooked prior to image formation by a factor L in azimuth and/or range direction. As can be seen in figure 5.1 there are numerous Radarsat-2 modes of operation available. The dataset available for testing in this project contains images acquired with the following modes of operations:

- Single Beam Standard: S6
- Single Beam Standard: S8
- ScanSAR Narrow: SCNA, SCNB
- ScanSAR Wide: SCWA, SCWB

Characteristics such as nominal swath width, pulse bandwidth, incidence angles, and sampling rates willl vary for the different modes [57]. Figure 5.5 and figure 5.6 illustrates how the single beam and scanSAR mode operates.

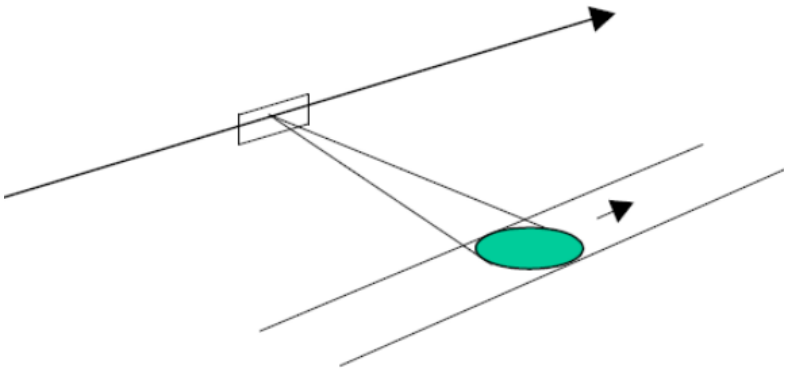

Figure 5.5: *Radarsat-2 single beam mode (figure from [57]).*

The data set contains ground range SAR products, that is, products that consists of data that has been projected to ground range. The two types of ground range products in the dataset are Path Image Plus (SGX) products and Path Image (SGF) products. The different single beam products and scanSAR products available and its characteristics are summarized in table 5.1 and table 5.2 [57].

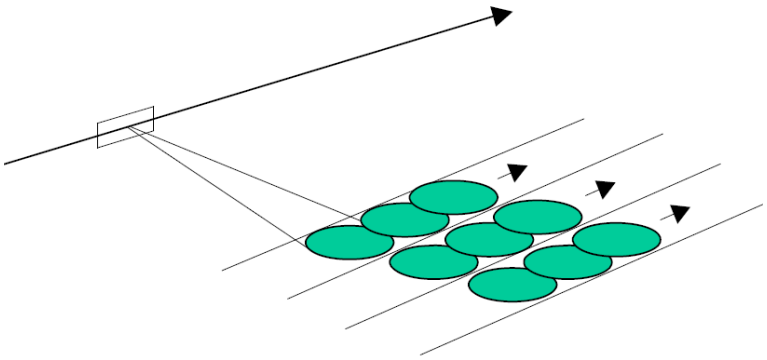

Figure 5.6: *Radarsat-2 scanSAR mode (figure from [57]).*

Table 5.1: Beam Mode: Standard

Characteristics	***SGX***	***SGF***
Pixel Spacing [rg×az] (m)	8 × 8	12.5 × 12.5
Nominal Resolution [rg×az] (m)	(26.8 – 17.3) × 24.7	(26.8 – 17.3) × 24.7
Nominal Incidence Angles (°)	20 to 52	20 to 52
Nominal Scene Size [rg×az] (km)	100 × 100	100 × 100
Number of Range Looks	1	1
Number of Azimuth Looks	4 with 39% overlap	4 with 39% overlap
Polarization Options	Single Co and Cross (HH,VV,HV,VH) Or Dual (HH + HV or VV + VH)	Single Co and Cross (HH,VV,HV,VH) Or Dual (HH + HV or VV + VH)

There are 8 different beam positions available for the Standard beam mode, ranging from S1 to S8. The incidence angles in table 5.1 range from 20° at the inner edge of S1 to 52° at the outer edge of S8. However, the available dataset contains products that have been acquired using S6 or S8, which is why the whole range of incidence angles in the above table is not available [57].

Table 5.2: Beam Mode: ScanSAR

Characteristics	*ScanSAR Narrow (SCNA, SCNB)*	*ScanSAR Wide (SCWA, SCWB)*
Pixel Spacing [rg×az] (m)	25 × 25	50 × 50
Nominal Resolution [rg×az] (m)	(81 – 38) × 60	(163 - 73) × 100
Nominal Incidence Angles (°)	20 to 46	20 to 49
Nominal Scene Size [rg×az] (km)	300 × 300	500 × 500
Number of Range Looks	2	4
Number of Azimuth Looks	2	2
Polarization Options	Single Co and Cross (HH,VV,HV,VH) Or Dual (HH + HV or VV + VH)	Single Co and Cross (HH,VV,HV,VH) Or Dual (HH + HV or VV + VH)

Most of the the products in dataset 2, with the exception of the SGX products, are undersampled. This means that not all of the information is preserved [57].

6

Results and Discussion

The aim of this project is to present an algorithm for estimating the radar cross section of the ocean background in SAR images. As explained in chapter 4.1 and 4.2, a dataset containing three gradient images was used to determine the frequency threshold that will be applied during lowpass filtering. The results of this frequency threshold evaluation will be presented in this chapter.

The goal is to truncate a portion of the highest intensities in real SAR images and then apply a NFFT algorithm to the truncated SAR data. The output from the NFFT algorithm should be frequencies on a regular grid and by utilizing a lowpass frequency filter, the underlying ocean radar reflectivity should be obtained. The implementation of the NFFT algorithm, as well as issues and results, will be studied in this chapter.

6.1 Frequency Threshold Evaluation

In order to study the frequency threshold that will be applied during lowpass filtering, dataset 1 was utilized. By plotting the different measures presented in chapter 4.2 (SSI, ENL, EPI, SSE) as a function of the threshold, a decision regarding the threshold can be made. From preliminary testing on the gradient images, it was decided that the threshold would be varied between $D_0 = 0$ to $D_0 = 60$ (see equation 4.1 and figure 4.2). Applying a threshold greater than 60 will result in an image where speckle is not sufficiently suppressed.

It was also found that applying a threshold below $D_0 = 5$ made the gradient images completely unrecognizable. The goal is to test the newly proposed algorithm on the products in dataset 2, which consists of products that have been multilooked a total of either four or eight times. Therefore, the shape parameter L for the simluated speckle was made to vary between $L = 4$ and $L = 8$. By doing so, it is possible to evaluate the effect of multilooking on the required frequency threshold.

It was observed that even though the number of looks (L) varied, the shape of the different lowpass performance plots (see figure 6.1 and figure 6.2) did not vary significantly. Figure 6.1 and 6.2 illustrates this fact. In figure 6.1 the gradient used to obtain the different measures is multiplied with simulated speckle with shape parameter $L = 4$. For figure 6.2, $L = 8$ was used. As can be seen, the value of the measures will vary, but the shape of the plots are quite similar. Therefore, one can conclude, that the same frequency threshold will be applied during lowpass filtering for products that have been multilooked with different number of looks. Additional tests were also executed on speckled gradient images that where simulated with shape parameter $L = 2$ and $L = 16$. These tests yielded the same results. Because of this and the fact that the majority of the products in dataset 2 are multilooked four times, $L = 4$ will be used as shape parameter when simulating speckle from now on.

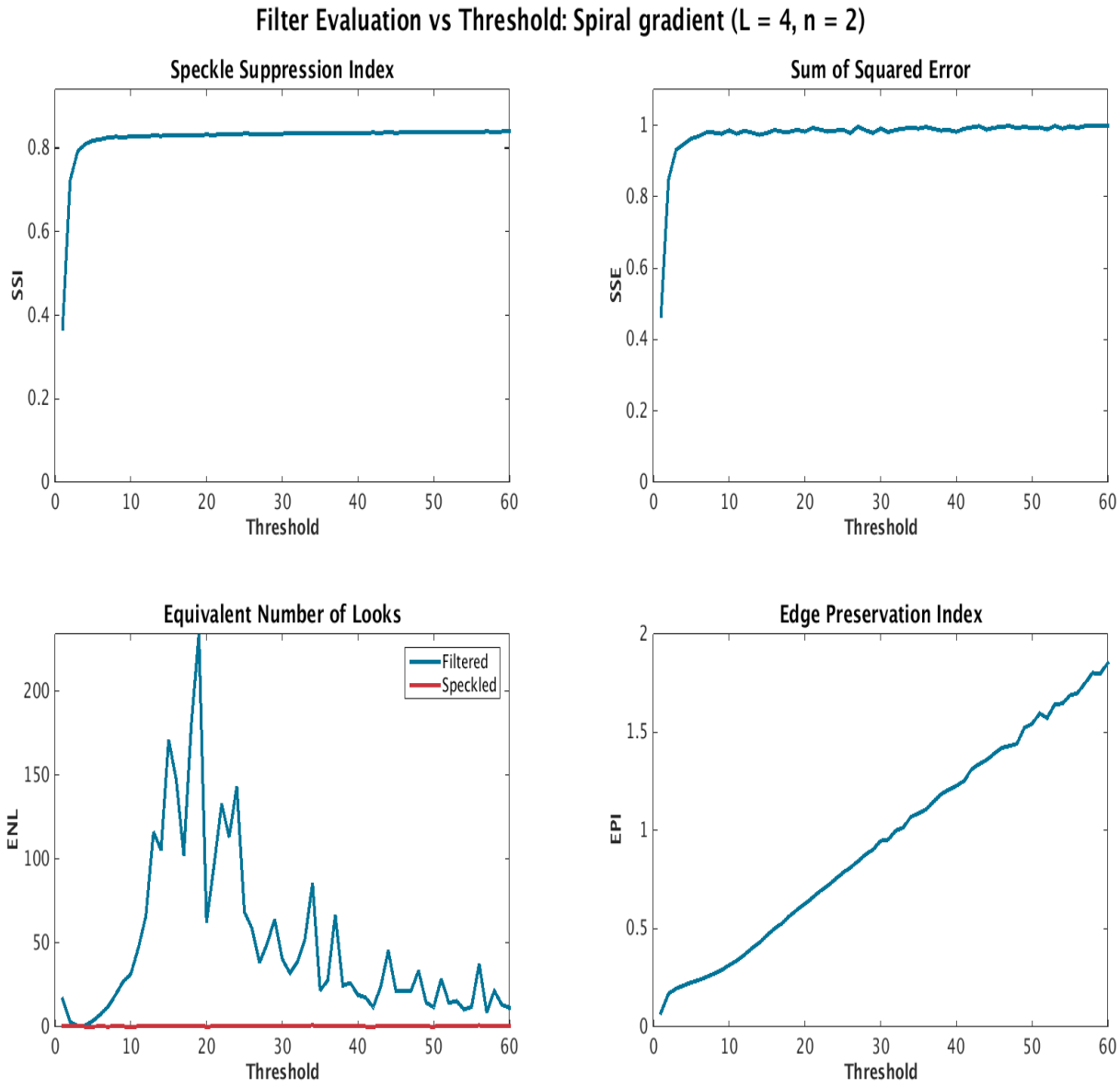

Figure 6.1: *Filter evaluation measures for the spiral gradient ($L = 4$). Evaluation measures present in the figure are: speckle suppression index, equivalent number of looks, sum of squared error, and edge preservation index.*

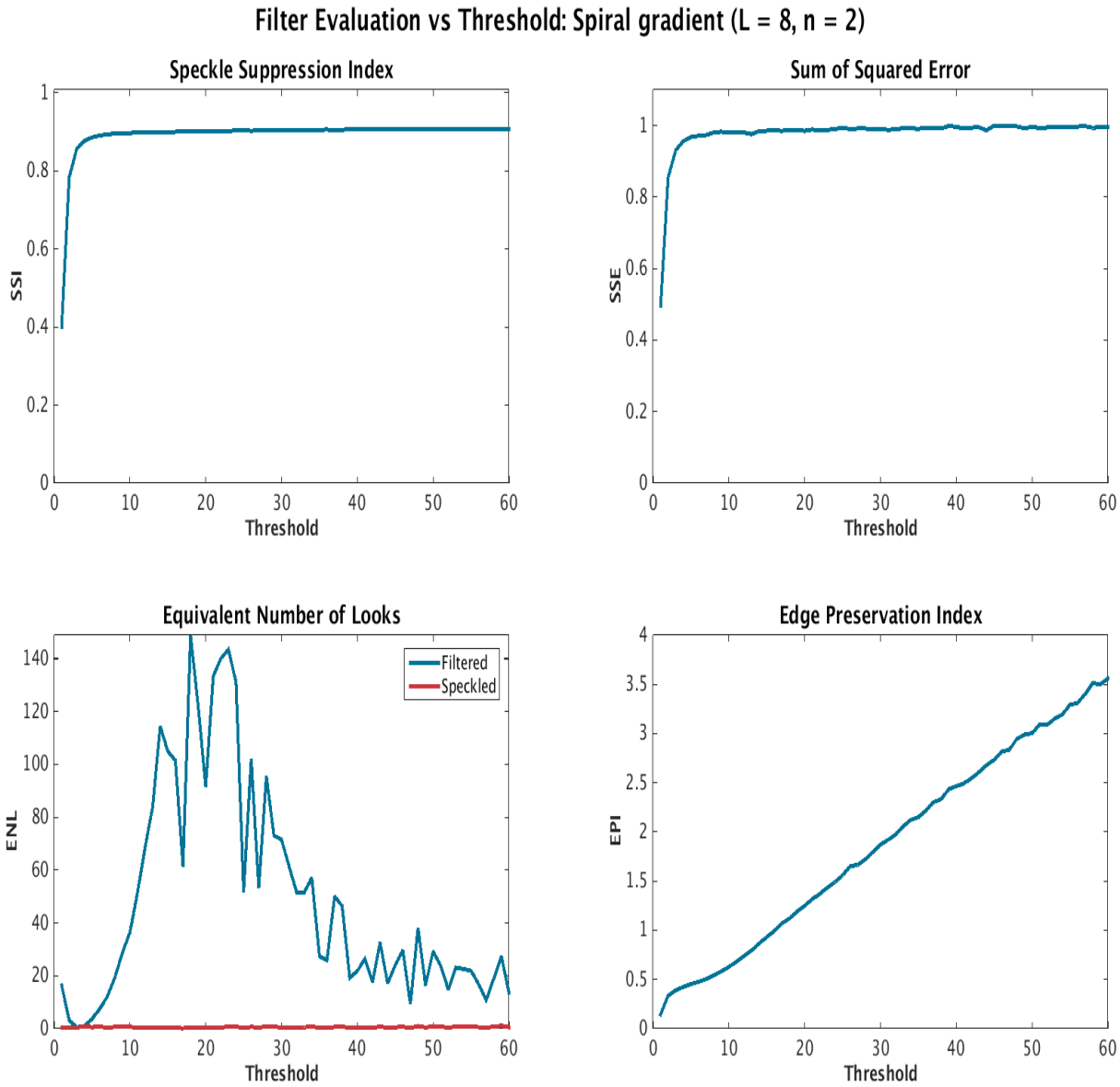

Figure 6.2: *Filter evaluation measures for the spiral gradient (L = 8). Evaluation measures present in the figure are: speckle suppression index, equivalent number of looks, sum of squared error, and edge preservation index.*

The optimal threshold value is scene dependent, which is why it is natural to want an adaptive algorithm that determines the threshold. Such an algorithm will require computation time, which means that the value must be balanced against the need for rapid estimation. Ideally, a fast automatic threshold algo-

rithm that depends on specific input parameters should be developed. Because of the need to balance conflicting requirements such as speckle suppression (smoothing) and preservation of details, the goal would be to express the contradictory requirements mathematically. If one could construct a mathematical function that depended on both the smoothing and the edge preservation requirements, it would be possible to find an optimal threshold. The problem is that it would be necessary to apply a weight to the different requirements in order to combine them and define the mathematical function correctly. These weights would have to be decided by subjective evaluation of each scene. For this project, a fixed threshold will be set based on both objective and subjective criteria.

The different evaluation measures presented in chapter 4.2 and in figures 6.7, 6.8, and 6.9 are objective criteria. It will be hard to make a decision concerning the frequency threshold only based on these. Therefore, some subjective criteria are needed. These will be in the form of average spectral profiles and intensity profiles. Visual examination of filtrered gradients, where a varying degree of thresholds have been applied, will also be of help when determining the threshold.

Next, in figure 6.4, figure 6.5, and figure 6.6, a visual result of applying three different thresholds are presented. The figures show the original gradient, the speckled gradient, three gradient images that have been filtered with different thresholds, and their corresponding spectral and intensity profiles. This will provide a visual insight into what the frequency threshold should be. The spatial location of the intensity profiles in the different gradients is illustrated in figure 6.3. When speckle is multiplied to each of the gradient images, a much larger portion of the images will contain high frequencies. Also, low frequencies will span a broader range in the frequency spectrum. This can be seen from the spectral profiles present in figures 6.4, 6.5, and 6.6.

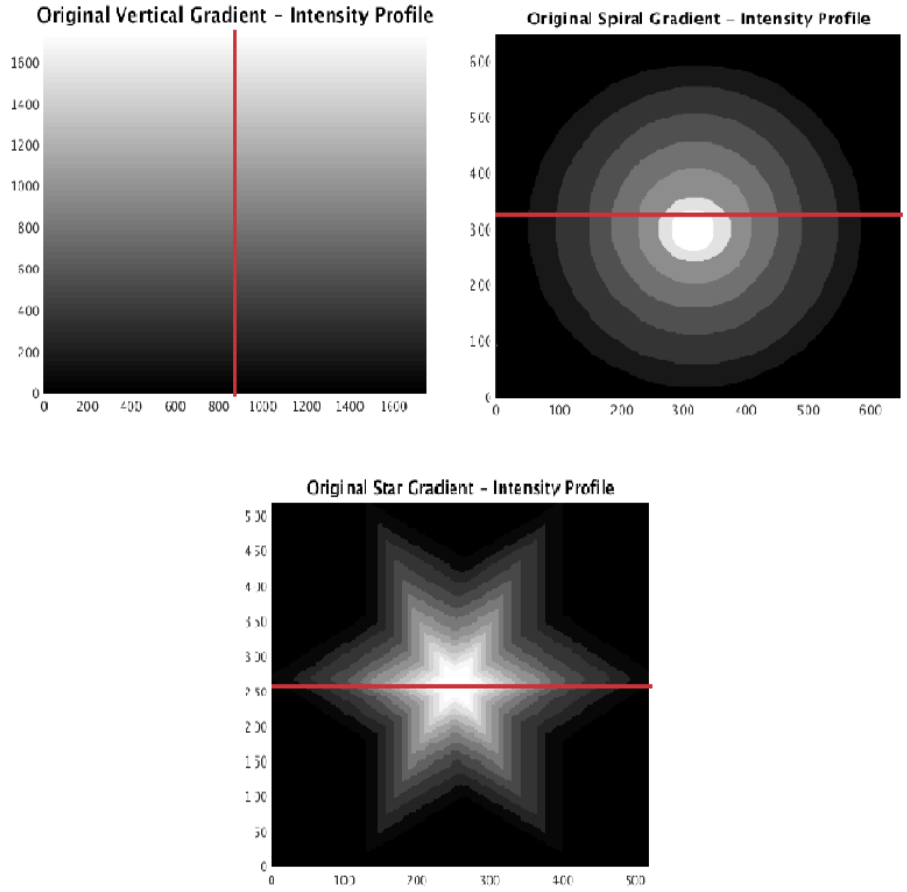

Figure 6.3: *Illustration of where the intensity profiles in each of the gradient images are located, represented by a red line in each of the three images.*

As can be seen in figure 6.4, the vertical gradient does not contain any edges. Therefore, applying a relatively low threshold will be sufficient. The intensity profile of the gradient filtered with $D_0 = 10$ is similar to the intensity profile of the original gradient. By visually inspecting the images, the same is true for the gradient images. By examining the spectral profile of the filtered image ($D_0 = 10$) and the spectral profile of the original image, it is clear that applying a greater threshold allow higher frequencies to be passed and more of the information in the original speckled gradient image is preserved. After filtering, false edges appear in the intensity profiles. These edges emerge at the top and bottom of the gradient. For a gradient image with no edges, a threshold of around 10 or 11 might suffice. However, the suspicion is that this threshold is too low for images containing edges.

Both the star and spiral gradient contain edges. The spiral gradient contains less edges than the star gradient and the edges are located closer together. Applying a threshold of $D_0 = 10$ will not be satisfactory for these two gradients. This is seen in both the image itself, and the spectral and intensity profile. The intensity profiles of the two gradients show that a threshold of $D_0 = 25$ will work better for images that contain edges. The same cannot be said for the spectral profiles. When applying a threshold of $D_0 = 25$, a relatively large portion of the original high frequency information is lost. As mentioned in chapter 4.2, suppressing speckle will require the attenuation of high frequencies, while edge preservation will require passing of the high frequencies. Therefore most of the information lost after thresholding is edge information. Filtering with a higher frequency threshold will allow a decrease in information loss. However, from examining the intensity profiles in figures 6.5 and 6.6, speckle is not sufficiently suppressed. This is why a tradeoff between speckle suppression and edge preservation is needed. After studying the spectral profiles, intensity profiles and images as a result of applying different thresholds, it appears that for images with edges, a threshold around $D_0 = 25$ and $D_0 = 30$ should be set.

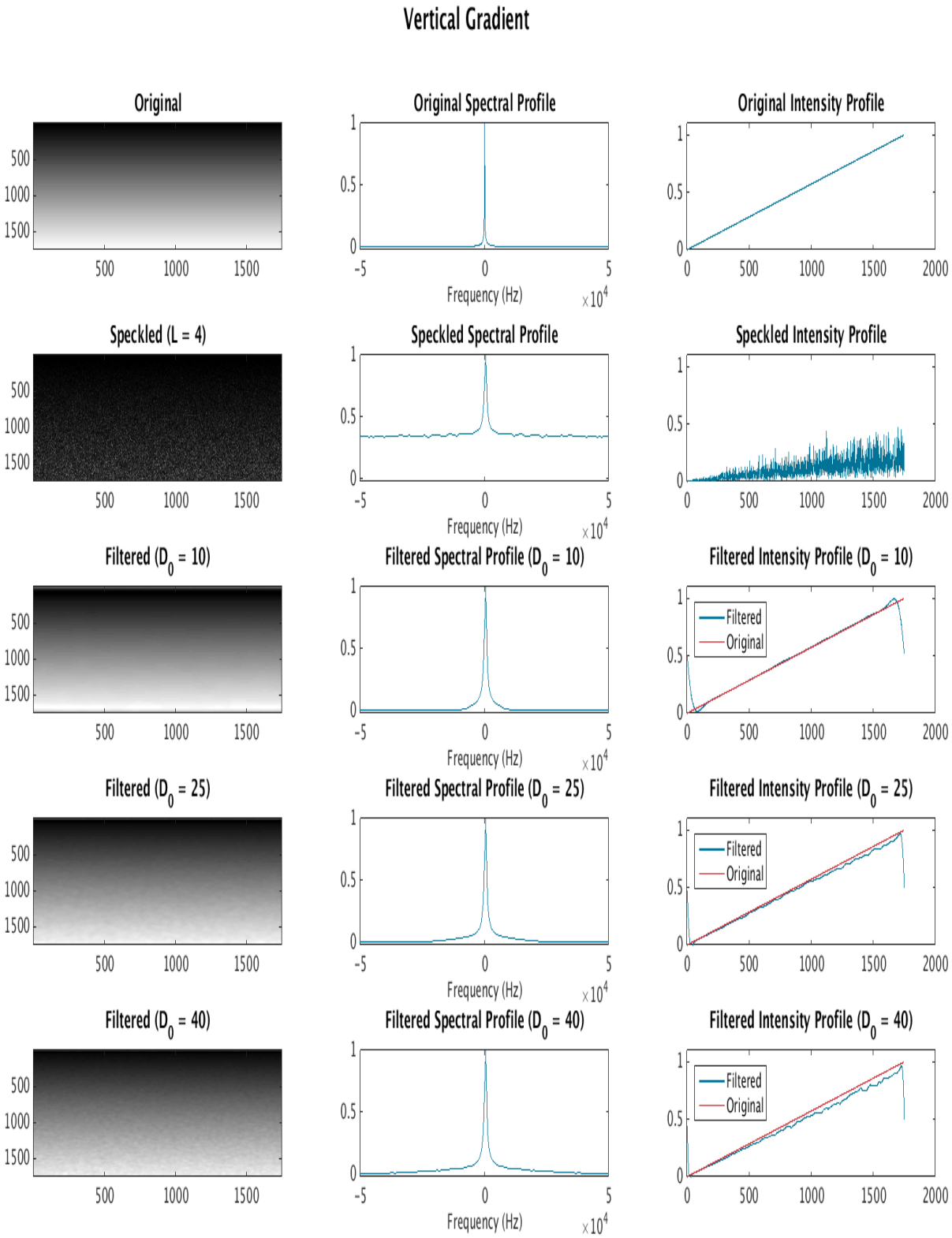

Figure 6.4: *Original vertical gradient, speckled gradient ($L = 4$), various filtered gradients ($D_0 = 10, 25, 40$) and their corresponding spectral and intensity profiles.*

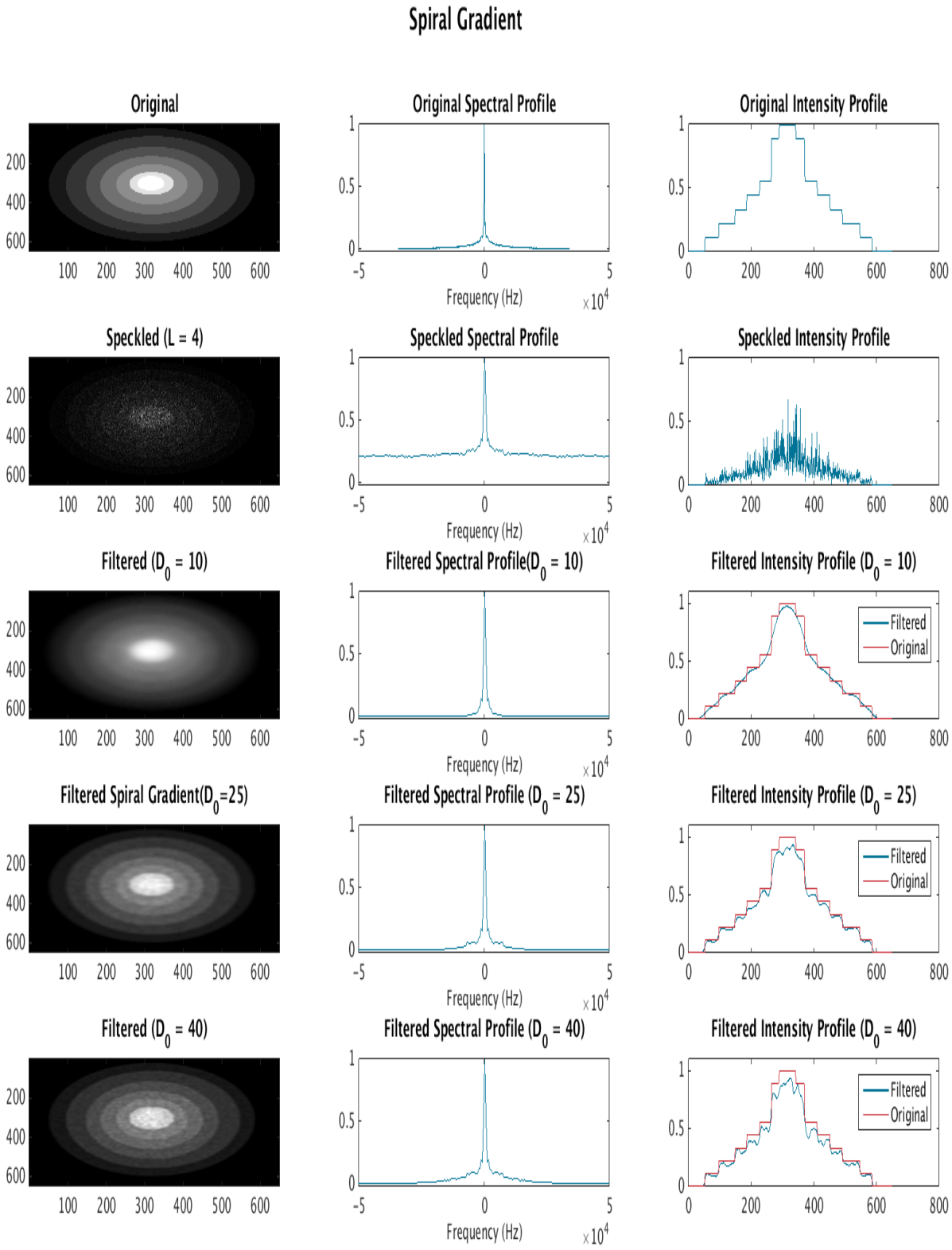

Figure 6.5: *Original spiral gradient, speckled gradient ($L = 4$), various filtered gradients ($D_0 = 10, 25, 40$) and their corresponding spectral and intensity profiles.*

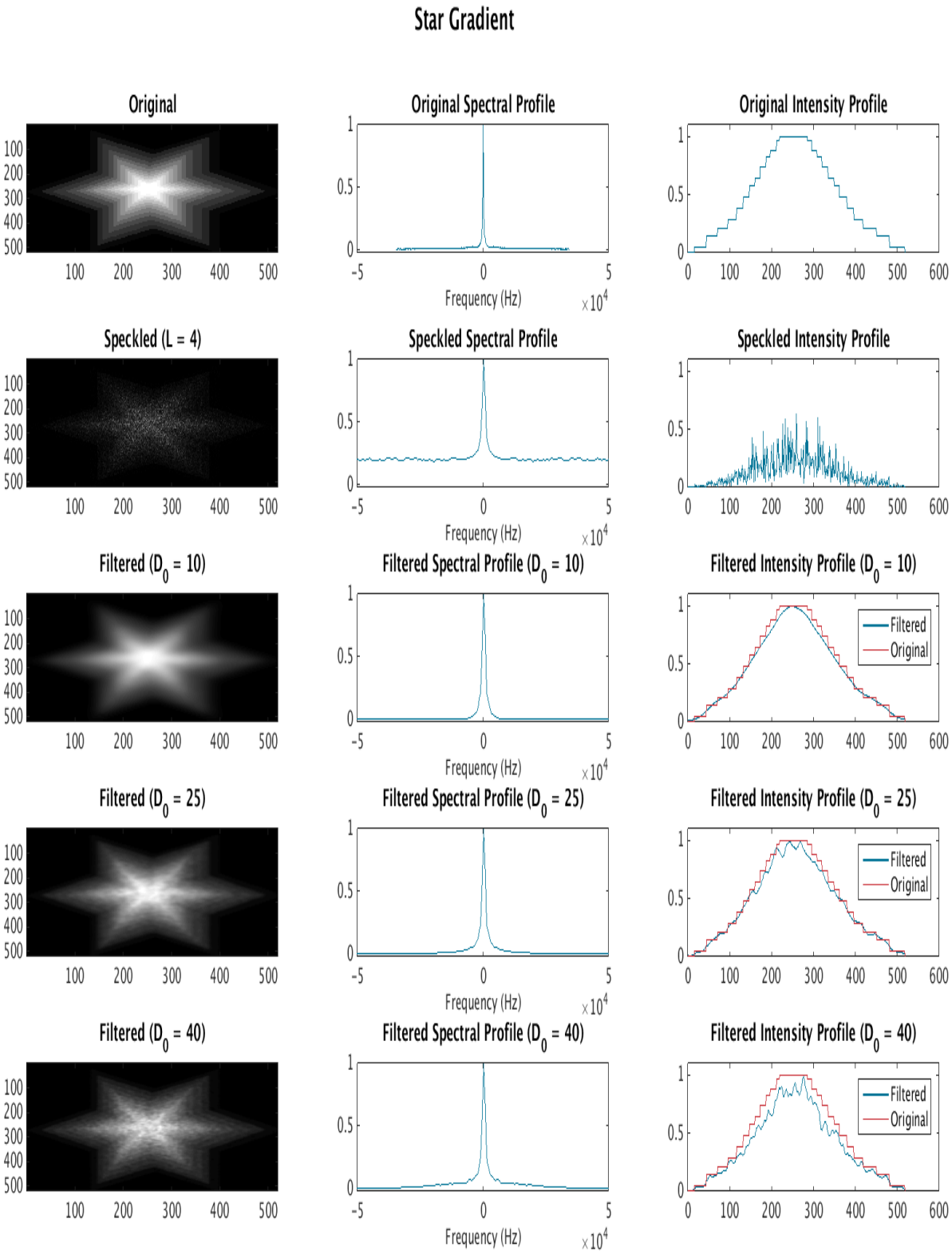

Figure 6.6: *Original star gradient, speckled gradient ($L = 4$), various filtered gradients ($D_0 = 10, 25, 40$) and their corresponding spectral and intensity profiles.*

The obective criteria to be considered when deciding a threshold are: speckle suppression index, equivalent number of looks, edge preservation index, and sum of squared error. These were all plotted as a function of thresholds, and they will contribute to determining a suitable threshold.

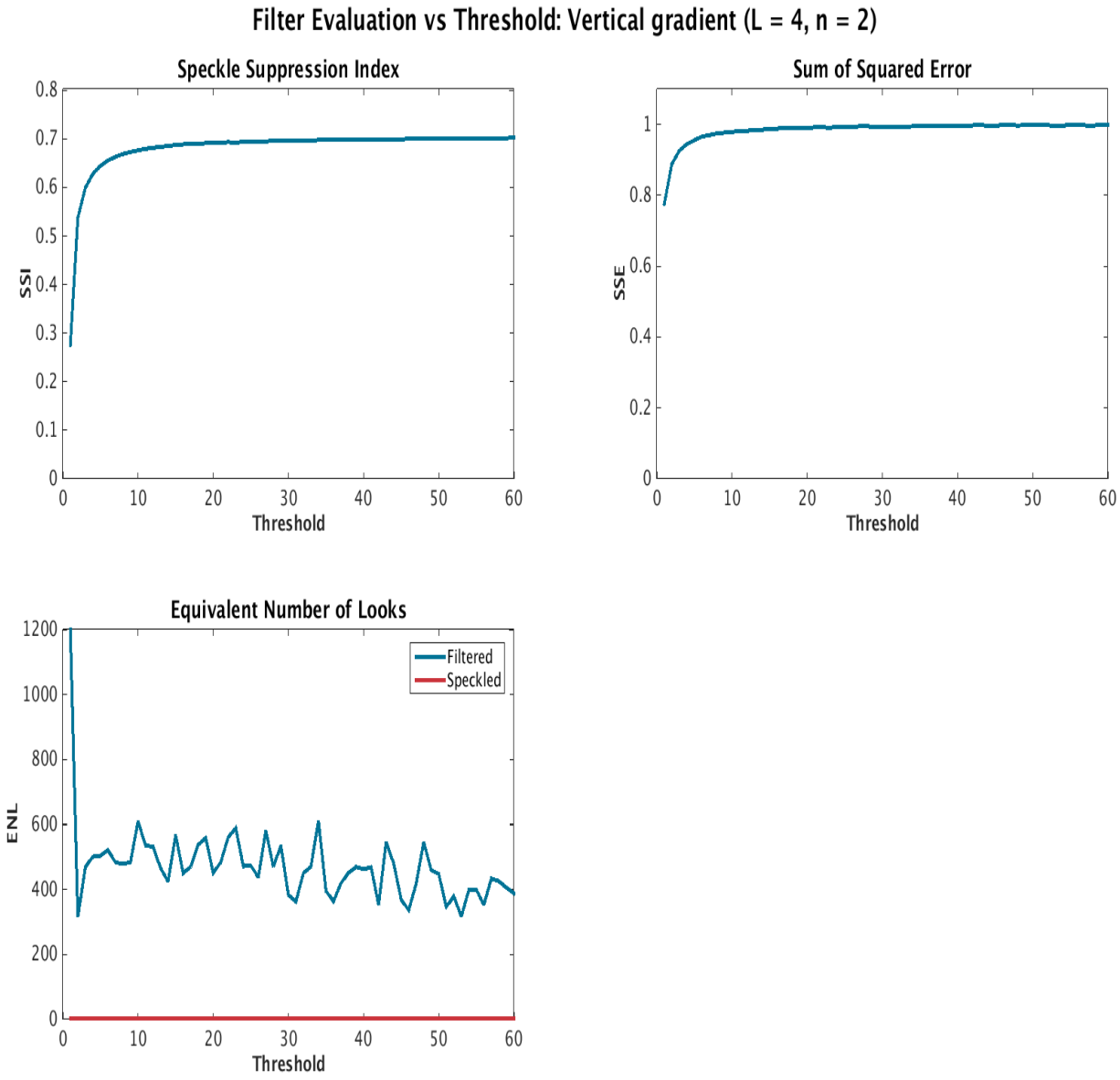

Figure 6.7: *Filter evaluation measures for the vertical gradient (L = 4). Evaluation measures present in the figure are: speckle suppression index, equivalent number of looks, and sum of squared error.*

As mentioned earlier, a lower value of the SSI indicates better speckle suppression. As can be seen in figures 6.7, 6.8, and 6.9, the SSI plot flattens out around threshold $D_0 = 10$. The same phenomena occurs for the SSE plots.

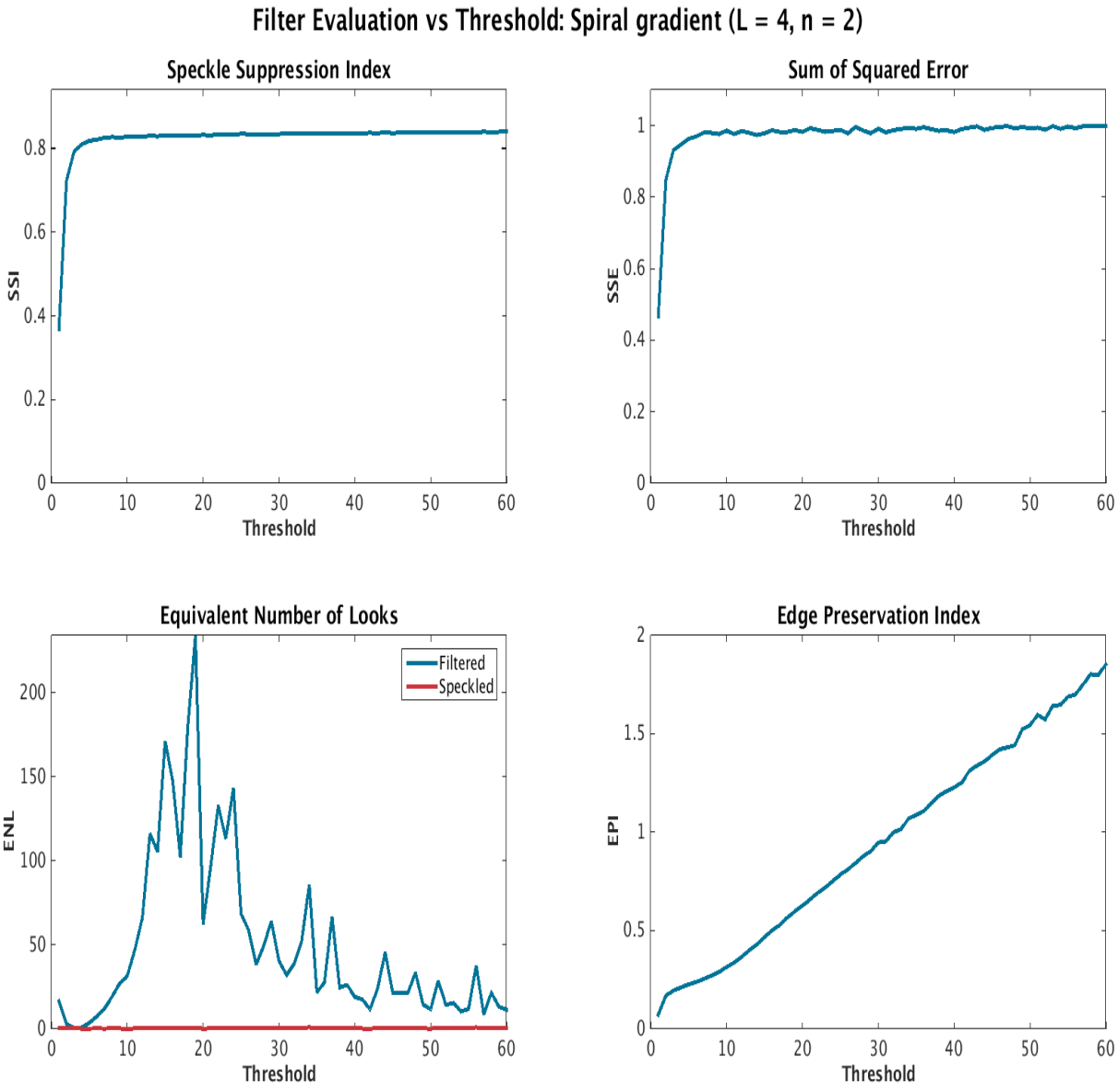

Figure 6.8: *Filter evaluation measures for the spiral gradient (L = 4). Evaluation measures present in the figure are: speckle suppression index, equivalent number of looks, sum of squared error, and edge preservation index.*

The ENL for the vertical gradient will act similar to the SSI and SSE. That is, it somewhat levels out at threshold around $D_0 = 10$. The same cannot be stated for the spiral and the star gradient. A higher ENL yields better speckle suppression. Judging from the ENL plots of the spiral and star gradient, a suitable threshold should exist in the range between $D_0 = 15$ and $D_0 = 25$. This is the interval where the ENL is greatest and thus, speckle suppression will be strongest here.

For the vertical gradient and thresholds below $D_0 = 10$, the ENL acts as expected, it is extremely high. For the remaining two gradients, it is very low. These two gradients contain structures and applying a threshold below $D_0 = 10$ will distort the image substantially. It is believed that the amount of distortion that occurs in images with structure will affect the statistics of the image itself. This explains the effect of applying a lowpass filter with a low threshold.

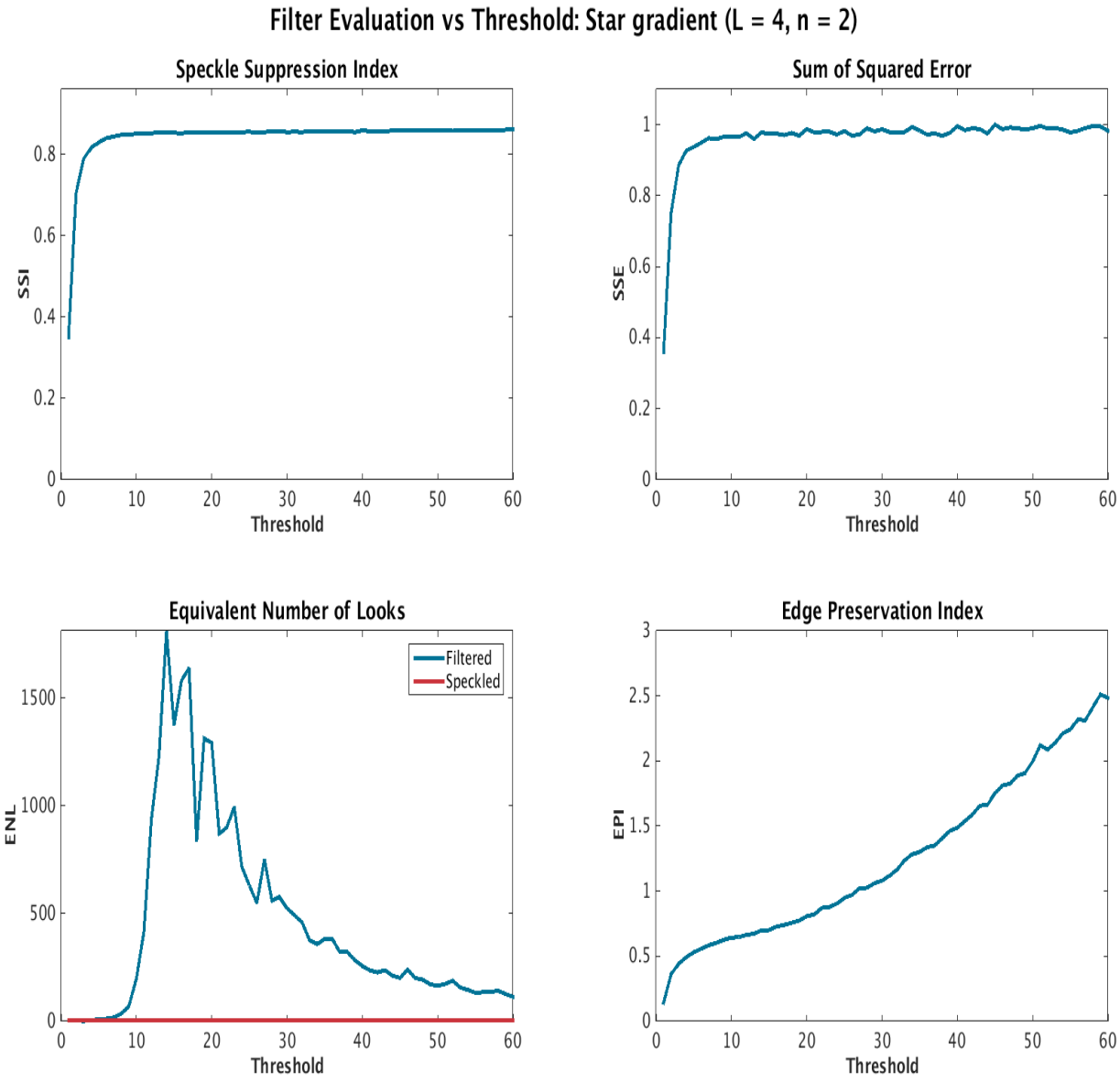

Figure 6.9: *Filter evaluation measures for the star gradient (L = 4). Evaluation measures present in the figure are: speckle suppression index, equivalent number of looks, sum of squared error, and edge preservation index.*

An EPI was calculated for the images containing speckle. Both of the EPI plots show relatively monotonically increasing functions, where a higher EPI value yields better edge preservation. These two plots, together with the plots for the ENL does not give a clear answer to what the threshold should be, but a

decision has to be made. Seeing as the acceptable ENL interval was considered to lie between $D_0 = 15$ and $D_0 = 25$, and the EPI should be as large as possible, the threshold is set to the upper limit of the acceptable ENL interval. Thus, it is reasonable to choose a threshold around $D_0 = 25$ based on the objective criteria. This decision coincides with the decision made based on the subjective criteria.

In order to substantiate this decision, a few supplementary tests were performed. They consisted of evaluating spectral and intensity profiles for thresholds between $D_0 = 23$ and $D_0 = 28$. The supplementary tests supported the decision made in the previous paragraph ans thus, the final threshold should be set to $D_0 = 25$. The effects of applying this threshold to the different gradients are illustrated in figures 6.4, 6.5, and 6.6.

6.2 NFFT

For this project, an existing software developed by Keiner et al. [46] was used. The NFFT 3 software library is primarily a C software library, but a MATLAB interface does exist., and this MATLAB interface was utilized in this thesis. The algorithm requires a number of different input parameters which were introduced in chapter 4.4. The overall goal of this project was to present an algorithm for estimating the underlying radar reflectivity of the ocean background, in which the NFFT was utilized. Therefore, it is necessary to evaluate whether or not the NFFT can be applied to truncated SAR data. The following defaults exist for the NFFT 3 software library [46] [58]

- Window function - Kaiser Bessel
- FFT length ($n = \alpha M$) - power of two such that $2 \leq \alpha < 4$
- Cut-off parameter (m) of the window function - For the Kaiser Bessel window, the default is 6

The choice of window function and cut-off parameter will have a direct influence on the accuray. The accuracy has already been sacrificed for rapid computation by choosing a lowpass filter in the frequency domain as a way to reduce speckle and therefore, the default values corresponding to the aforementioned input values will not be altered. Unless a situation arises that requires the oversampling factor and the FFT length to be altered, the default values will remain as defined. When the area of missing datapoints that needs to interpolated is large, an increased FFT length and oversampling factor might have to be utilized.

As mentioned throughout the thesis, the goal is to develop a fast algorithm that will handle situations with multiple targets and heterogeneous ocean clutter. Traditionally, algorithms that are able to handle such situations, are not very fast. The key points of the proposed algorithm were summarized in figure 4.1 in chapter 4 and it is clear that the majority of the algorithm relies on the nonuniform FFT and how it performs in regards to truncated SAR data.

The NFFT algorithm was implemented using the exisiting NFFT 3 MATLAB interface. Input parameters that needs to be defined are the nonequispaced nodes $\boldsymbol{x}$ and the Fourier coefficients f. The input parameter f is defined as the truncated SAR image and the nodes are based on whether or not the SAR data has been truncated and if so, the truncation method applied. There are two ways in which the truncated data can be defined. One way is to find the maximum value of the data, and setting an intensity threshold based on this value. The threshold can be determined by deciding the percentage of highest intensities that is to be truncated, and thus only including pixels that have a value less then the determined threshold. Another way in which the truncated SAR image can be defined is by first ranking all of the intensity values of the pixels from minimum to maximum, before removing a certain amount of the highest intensity pixels. The first approach of defining the truncated data, was applied for the purpose of this project.

As mentioned in chapter 3, targets will appear as high intensity pixels on an otherwise dark background. The backscatter from targets and what parameters it depends on, was also discussed. Some target pixels will have intensity values that are considerably greater than the intensity values of the surrounding ocean. Other target pixels might be embedded in speckle and thus the contrast between target pixels and ocean background pixels will be low. Because of this, distinguishing an ocean pixel from a target pixel might prove difficult. Therefore, determining a truncation threshold will not be straightforward. In the truncation process, high intensity targets pixels as well as pixels belonging to the ocean will be removed. Hence, it is necessary to compensate for the unwanted energy loss that occurs in the process of truncation.

First, the NFFT algorithm was tested on a SAR image from the second dataset. The first test yielded unsatisfactory results and the following sections describe and discuss problems and issues that arose during testing. In order to gain better control of the input and output, a Shepp-Logan phantom image was created in MATLAB. By performing tests on the Shepp-Logan phantom image instead of real SAR data, like the Radarsat-2 dataset presented in chapter 5, it will be easier to evaluate the results obtained. The symmetry of the phantom image makes it possible to better assess geometric distortions, such as rotation and shifting. This phantom image is a grayscale intensity image that consists of one large ellipse and several smaller ones. The image is supposed to act as

a model of the human brain and features within it [59].

The phantom image was used as input during debugging and evaluation of the NFFT algorithm. The phantom image is an image that has been used previously in articles addressing NFFT, specifically in regards to medical imaging such as magnetic resonance imaging (MRI) reconstruction [60]. The Shepp-Logan phantom image is shown in figure 6.10.

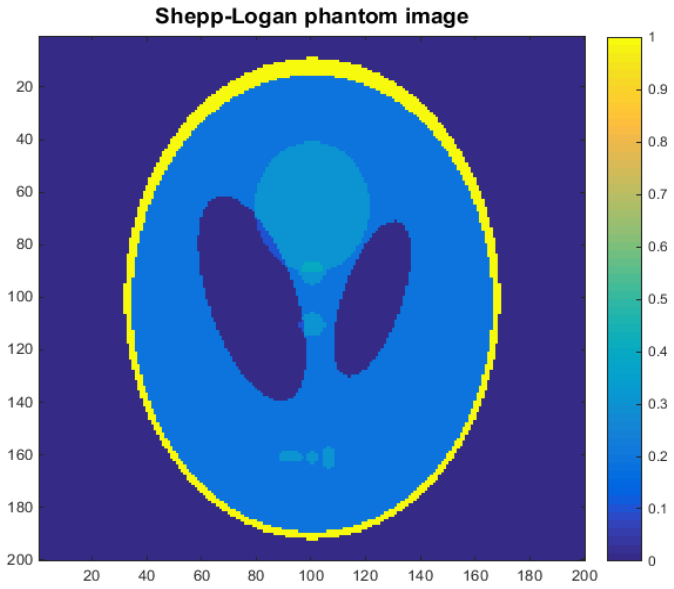

Figure 6.10: *Shepp-Logan phantom grayscale intensity image of size* 200×200.

The results of running the NFFT algorithm with the phantom image as input is shown in figure 6.11. Pixels with value equal to one (corresponding to yellow in figure 6.10) were truncated from the original image. As can be seen, the spatial image obtained from the NFFT algortihm is completely distorted and the algorithm clearly does not perform as planned. In order to pinpoint what went wrong, the following test were executed:

- Use an untruncated phantom image as input to check whether or not a reconstructed image is obtained.
- Evaluation of the nonequidistant nodes.
- Perform a direct computation of the nonuniform discrete Fourier transform (NDFT) and evaluate the results.

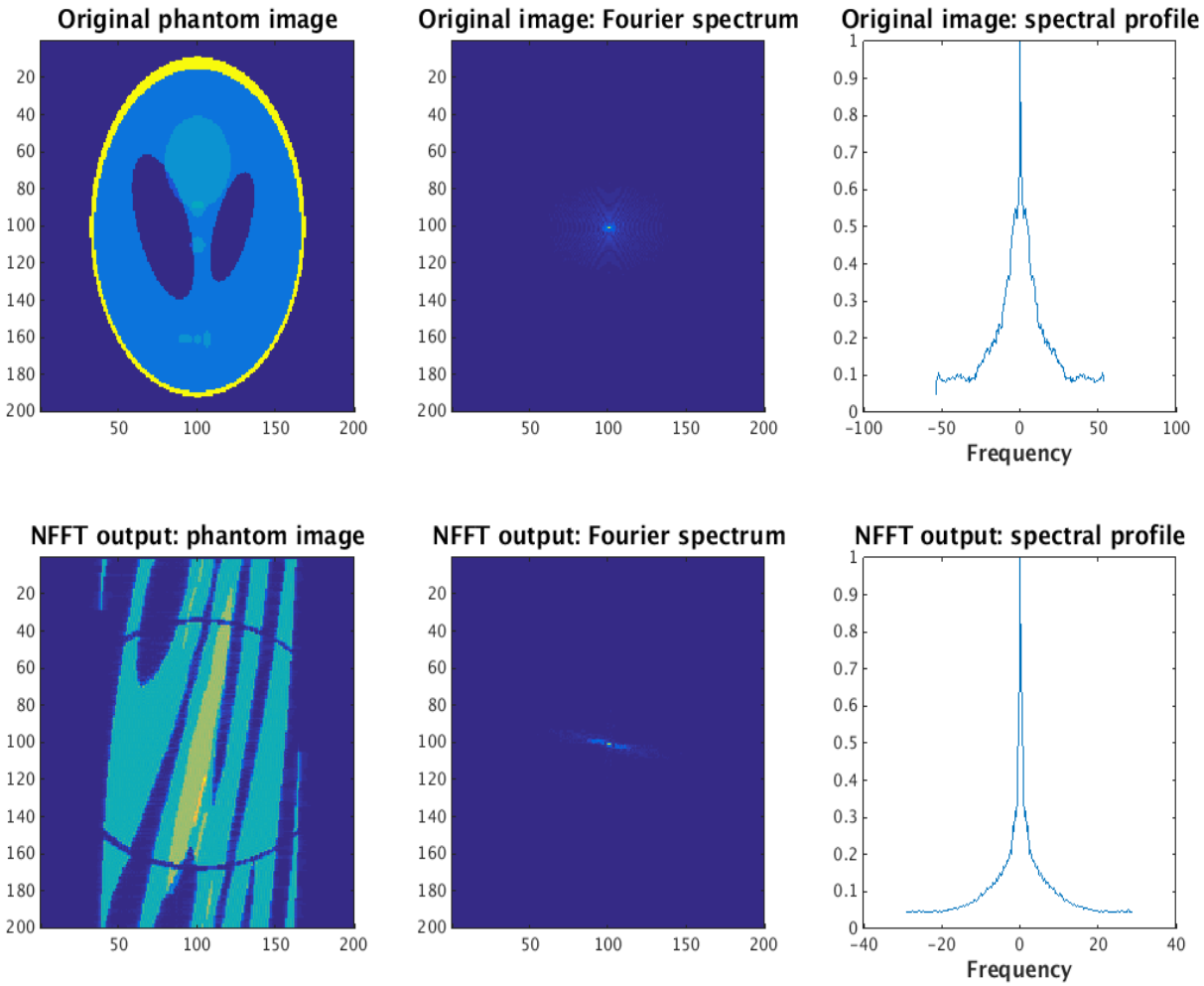

Figure 6.11: *Result from NFFT algorithm with truncated phantom image as input.*

6.2.1 Untruncated SAR data

When the NFFT algorithm failed to deliver the results needed for the proposed algortihm, the first step was to evaluate the performance of the NFFT algorithm when using untruncated data as input. Will the output be a reconstructed version of the input data?

The NFFT 3 software contains two types of NFFT algorithms that are essential for this thesis. For the sake of simplicity, let's call them the forward NFFT and

the backwards NFFT. The forward NFFT takes the regular grid, $fhat$, as input, as well as nodes x. These nodes can be both equidistant and nonequidistant. The backwards NFFT, which is the algorithm described in chapter 4.4, can take either a regular grid or an irregular grid as input, as well as nodes that can be both equidistant or nonequidistant. The forward NFFT consists of the same three steps as the ones described for the backwards NFFT, only in reverse order.

In order to test whether or not the algorithm was able to reconstruct the original image when no truncation had been done, two tests were done. The input and output of the different tests were as follows:

1. A phantom image of size $N_1 \times N_2$ was used as input in the forward NFFT algorithm. Nodes were set to contain all datapoints within the input data. The output was a regular grid of frequencies with size $N_1 \times N_2$, which served as input for the forward NFFT algorithm. Nodes were still set to contain all datapoints within the current input data. The output was a regular grid in the spatial domain of size $N_1 \times N_2$.

2. A phantom image of size $N_1 \times N_2$ was used as input in the backwards NFFT algorithm. Nodes were set to contain all datapoints within the input data. The output was a regular grid of frequencies with size $N_1 \times N_2$, which served as input for the forward NFFT algorithm. Nodes were still set to contain all datapoints within the current input data. The output was a regular grid in the spatial domain of size $N_1 \times N_2$.

Figure 6.12 summarizes the two steps just described.

The results of the two test are shown in figure 6.13 and in figure 6.14. The figures show that the NFFT algorithms were able to reconstruct the input image completely with all information preserved. This indicates that the algorithm does in fact work and that the input parameters are defined correctly. The two test performed in the current section is equivalent to applying MATLAB functions *fftshift(fft2(·))* and *ifftshift(ifft2(·))* to the input image.

The next step towards solving the problem is to evaluate the nonequidistant nodes, which will be covered in the next section.

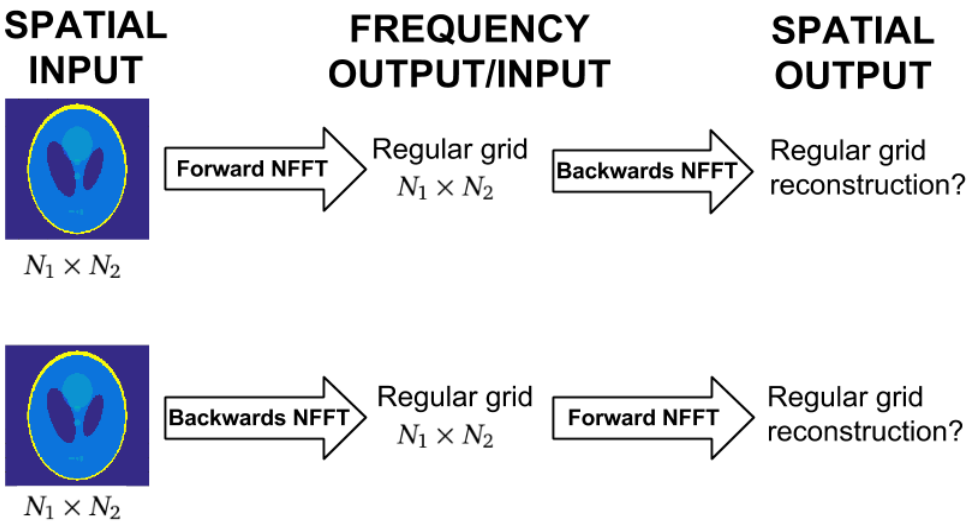

Figure 6.12: *An illustration of the two tests performed in the current section.*

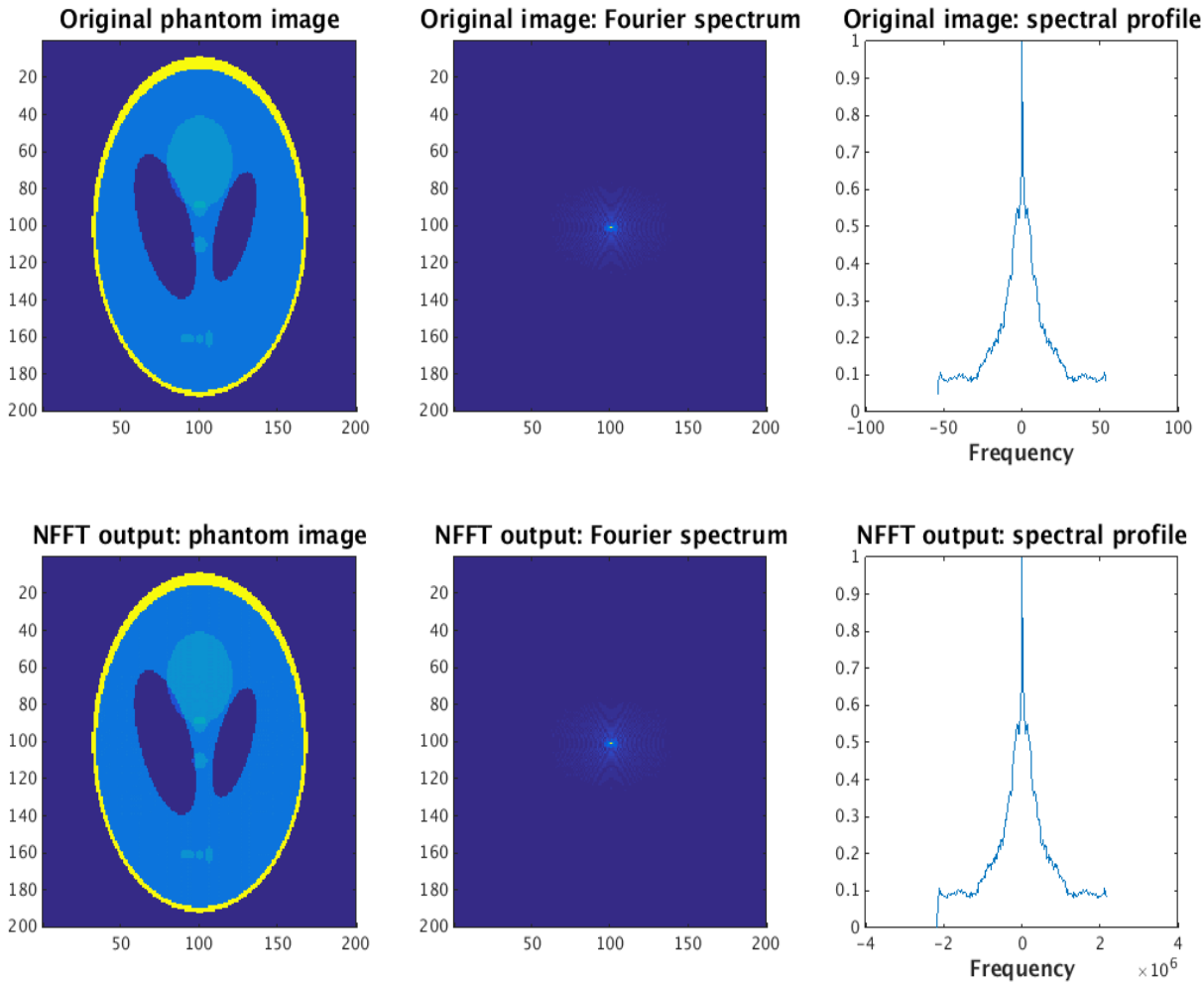

Figure 6.13: *Result from the NFFT algorithm with an untruncated phantom image as input and nodes set to contain all data points within the input data. First the forward NFFT was run, then the backwards NFFT with input set to be the output from the forward NFFT. The top row represents the original input phantom image, while the bottom row represents the results obtained from the current test. As can be seen, the image was completely reconstructed with all inofrmation preserved.*

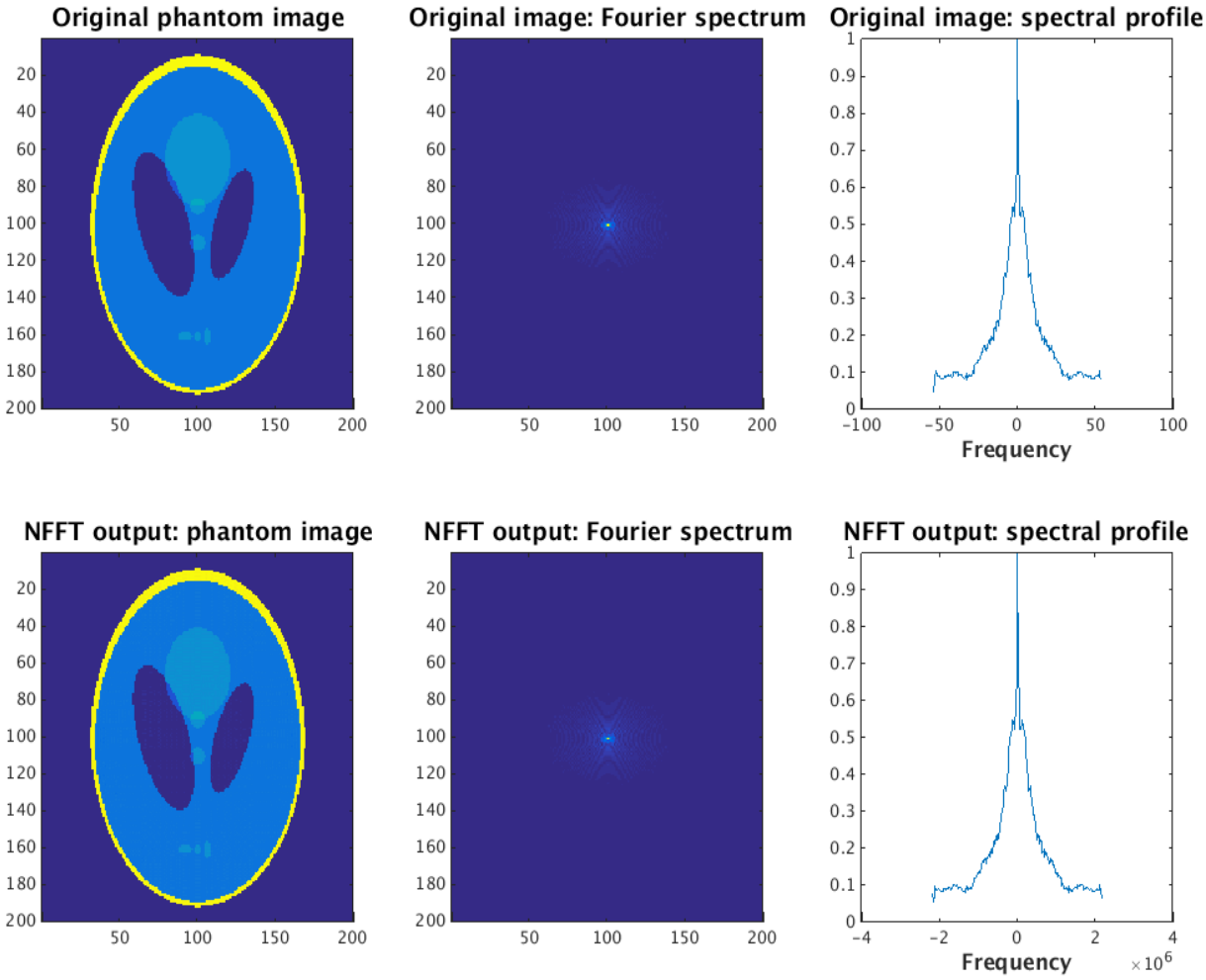

Figure 6.14: *Result from the NFFT algorithm with untruncated phantom image as input and nodes set to contain all data points within the input data. First the backwards NFFT was run, then the forward NFFT with input set to be the output from the backwards NFFT. The top row represents the original input phantom image, while the bottom row represents the results obtained from the current test. As can be seen, the image was completely reconstructed with all inofrmation preserved.*

6.2.2 Nonequidistant nodes

The current section will deal with the interpolation ability and nonequidistant nodes. Because of the results obtained from the previous section when no

truncation was performed , as well as the results obtained when truncation was applied, it was necessary to take a close look at the nonequidistant nodes. The initial hypothesis was that the NFFT algorithm would be able to interpolate relatively large blocks of data. When possible targets and their associated artefacts are truncated from the input SAR image, relatively big blocks of data will be removed. This is because targets in a SAR image might cover several pixels and their corresponding artefacts (e.g., sidelobes) will be extended throughout the scene. Therefore, it is required that the NFFT algorithm can handle such situations. In order to determine whether or not the NFFT software could handle truncated data at all, a different approach was taken in regards to defining the input nodes. Instead of truncating large blocks of data, a certain amount of stand-alone pixels ($\approx$ 5% for the current test) were removed from the data set, creating an irregular grid which would be used as input to the backwards NFFT. The results of this test is illustrated in figure 6.15.

From comparing figure 6.11 and figure 6.15 it is clear that the algorithm does not handle input images that have had big blocks of data removed from its dataset. The output image in figure 6.15 was not distored like the results in figure 6.11, which suggests that it is necessary to define nodes as described in the previous paragraph. Altering some of the input parameters, such as the oversampling factor and the FFT length might result in an algoithm that better handles the type of truncation that is needed in this thesis. However, from the results in this section, it is evident that the interpolation is not done as desired. Instead of interpolating at locations where data is missing, with the help of neighboring datapoints, it seems as though the location of the missing data is replaced with a zero value or at least an extremely low value. Therefore, altering some of the input parameters will serve no purpose.

Because this thesis is interested in situations with nonuniform spatial samples, no testing of the NFFT in regards to nonuniform frequency samples was performed.

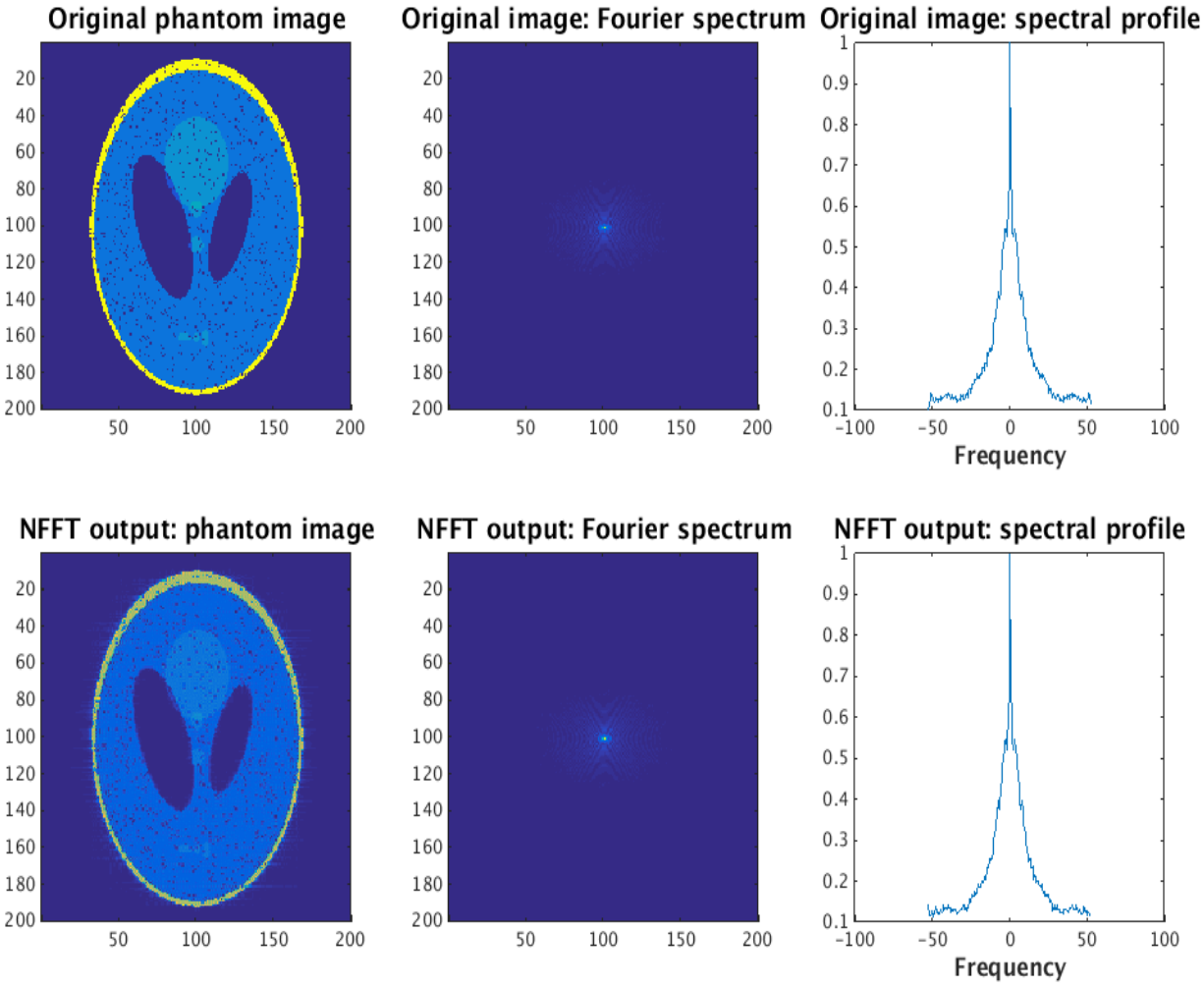

Figure 6.15: *Result from the NFFT algorithm with untruncated phantom image as input and nodes set to contain all data points within the input data. First the backwards NFFT was run, then the forward NFFT with input set to be the output from the backwards NFFT. As can be seen, the image was completely reconstructed with all inofrmation preserved.*

6.2.3 Direct Computation

The final test that was performed with respect to the NFFT was to compute the NDFT directly. Similarly to the previous section, a certain amount of stand-alone pixels ($\approx$ 5% for the current test) were truncated from the phantom image (see figure 6.15) before it was reshaped to a vector. Thus, the direct computation

of the NDFT at given nonequispaced nodes x_k, is defined as computing the following summation

$$F(u) = \sum_{k=1}^{M} f_k e^{-j2\pi u x_k / M} \tag{6.1}$$

where $u = -M/2, \ldots, M/2 - 1$. The computation of equation (6.1) provided results similar to the results obtained in the previous section (see figure 6.15). That is, the results were not as desired.

The summation of equation (6.1) requires significantly more time so even if the results had been satisfactory, computing the NDFT directly will not be a viable solution for the problem at hand.

Because of the undesired results obtained during the testing of the NFFT algorithm, a complete algorithm is not presented here. The NFFT has previously been utilized in areas like medical imaging, seismic analysis, and remote sensing. In remote sensing, the algortihm has been applied to SAR focusing algorithms. However, little attention has been made towards applying the NFFT to nonequidistant spatial samples.

7 Conclusion

The main goal of this thesis was to present a fast and robust algorithm for estimating the underlying radar reflectivity of the ocean. The proposed algorithm is meant to handle difficult scene situations and is primarily based on the NFFT. Therefore, it relies heavily on whether or not the NFFT algorithm provides the desired output for truncated SAR data. The matlab interface of the NFFT 3 software library was utilized, and the results were disappointing. After analyzing the results from the NFFT algorithm, it was concluded that the NFFT algorithm failed for the purpose of this thesis. Because of this, it was not possible to present a complete algorithm and discussions on matters such as truncation amount and energy compensation due to truncation remains to be evaluated.

A study on the frequency threshold was also performed in this thesis. After evaluating both subjective and objective criteria, a decision was made concerning the threshold of the lowpass filter. It was concluded that a threshold of $D_0 = 25$ would be applied during implementation of the proposed algorithm.

7.1 Future work

There are several areas in which further work can be recommended, mainly, an alternative approach to the NFFT algorithm. Even though the NFFT algorithm implemented in this project did not deliver the desired results, the development

of a fast and robust algorithm for the underlying radar reflectivity of the ocean continues to be of great interest. Other NFFT software libraries in combination with alternative interpolation schemes are available. These libraries might be worth trying out as a basis for alternative implementations of the NFFT algorithm. However, seeing as most of them are based on the theory presented in chapter 4.4, a different approach to the NFFT should be evaluated first.

An alternative approach to transforming data on an irregular grid is using wavelets. As mentioned in chapter 4.4, the basis functions of the Fourier transform are sinusoids. That is, every given signal can be represented as the sum of sinusoids. The wavelet transform on the other hand, have small waves or wavelets as basis functions [29]. Wavelets are often thought of as building blocks of functions, which allows fast computation and efficient representation. Also, wavelets are described as being represented in both time and frequency, which allows one to investigate both the time and frequency content of a given signal.

Traditionally, wavelet function $\psi_{j,m}$ are defined as translates and dilates of a so-called mother wavelet ψ. By varying j, different frequency ranges will be covered. The variable m defines the time shift. Such wavelets are referred to as first generation wavelets, and the Fourier transform is utilized for construction. Second generation wavelets are wavelets that are not necessarily translates or dilates of a given mother wavelets, which suggests that the Fourier transform cannot be utilized for construction. Instead, the lifting scheme, which is a method for constructing second generation wavelets, is used [61][63]. Wavelets are used in a variety of different areas, and second generation wavelets with a lifting scheme can be utilized for transforming data on an irregular grid. Therefore, they are of great interest for the purpose of futher development of the main idea of this thesis. A thorough step by step review can be found in [62], while the lifting scheme for constructing second generation wavelets is reviewed in [63]. Wavelets on irregular point sets is adressed in [64].

A relatively large portion of this thesis focused on determining a suitable threshold for the lowpass filter in the frequency domain. The threshold was determined from both objective and subjective criteria, and the results serve as a valuable basis for future studies. An adaptive thresholding scheme should be evaluated further.

When truncating the SAR image, high intensity pixels belonging to the ocean background will also be removed. This will cause the recovered mean intensity to be biased, which is why it is imperative to compensate for the energy lost in the truncation process. Also, determining an optimal truncation measure will give rise to a powerful algorithm. An optimal truncation measure should be determined based the statistics of the ocean image.

Eventually, the algorithm should be tested on real SAR data, like the data presented in chapter 5 of this thesis. The results from the algorithm should also be tested against previously described CFAR algorithms and the computational efficiency must be verified.

Bibliography

[1] Tao, D., S.N. Anfinsen and C. Brekke: A ship detection algorithm based on truncated statistics, Proc. EUSAR 2014, Berlin, Germany, 4 pp., 3-5 June, 2014

[2] Chuvieco, E., Huete, A., et al. (2009). Fundamentals of satellite remote sensing. CRC Press Inc.

[3] Cumming, I. G., & Wong, F. H. (2005). Digital Processing Of Synthetic Aperture Radar Data: Algorithms And Implementation (Artech House Remote Sensing Library).

[4] Natural Resources Canada, Tutorial: "Fundamentals of remote sensing"
http://www.ccrs.nrcan.gc.ca/resource/tutor/fundam/index_e.php

[5] Van Zyl, J., & Kim, Y. (2011). Synthetic aperture radar polarimetry. John Wiley & Sons.

[6] Elachi, C., Zyl, J.V., "Introduction to the physics and techniques of Remote Sensing", second edition, John Wiley & Sons, Inc., 2006

[7] Oliver, C., Quegan, S., "Understanding synthetic aperture radar images", SciTech Publishing, 2004

[8] Skolnik, M. I. (1962). Introduction to radar. Radar Handbook, 2.

[9] Knott, E. F. (2006). Radar cross section measurements. SciTech Publishing.

[10] Radar tutorial:
http://www.radartutorial.eu/01.basics/Radar%20Cross%20Sec

tion.en.html, April 2015

[11] Lee, J., Pottier, E., "Polarimetric Radar Imaging: From basics to Applications", CRC Press, 2009

[12] G. Engen and H. Johnson "SAR-ocean wave inversion using image cross spectra", IEEE Trans. Geo sci. Remote Sensing, vol. 33, pp.1047 -1056 1995

[13] Lee, J. S., Jurkevich, L., Dewaele, P., Wambacq, P., & Osterlinck, A. (1994). Speckle filtering of synthetic aperture radar images: a review. Remote sensing Reviews, 8(4), 313-340

[14] Qiu, F., Berglund, J., Jensen, J. R., Thakkar, P., & Ren, D. (2004). Speckle noise reduction in SAR imagery using a local adaptive median filter. GIScience & Remote Sensing, 41(3), 244-266.

[15] Rees, W.G., "Physical Principles of Remote Sensing", third edition, Cambridge University Press, January 2013

[16] Greidanus, H., "Satellite Imaging for Maritime Surveillance of the European Seas", in: "Remote Sensing of the European Seas" (ed. Barale, V., Gade, M.), Springer Science + Business Media B.V., 2008

[17] Crisp, D.J., "The State-of-the-Art in Ship Detection in Synthetic Aperture Radar Imagery.", DSTO Information Sciences Laboratory, Australia, May 2004

[18] Cloude, S.R., "Polarisation applications in remote sensing", Oxford University Press, 2010

[19] Staglianò, D., Lupidi, A., Berizzi, F., "Ship detection from SAR images based on CFAR and Wavelet Transfom", in Advances in Radar and Remote Sensing (TyWRRS), 2012 Tyrrhenian Workshop on, pp. 53-58, 2012.

[20] Vachon, P.W., Wolfe, J., "Validation of ship signatures in Envisat ASAR AP mode data using AISLive, Data acquisition, processing, and analysis results", Defence Research and Development Canada, Ottawa, March 2008

[21] Scharf, L. L. (1991). Statistical signal processing (Vol. 98). Reading, MA: Addison-Wesley.

[22] S. N. Anfinsen , A. P. Doulgeris and T. Eltoft "Estimation of the equivalent number of looks in polarimetric SAR imagery", Proc. IEEE IGARSS, vol. 4, pp.487 -490 2008

[23] Oliver, C. J., & Lombardo, P. (1996, December). Simultaneous mean and texture edge detection in SAR clutter. In Radar, Sonar and Navigation, IEE Proceedings- (Vol. 143, No. 6, pp. 391-399). IET.

[24] Rohling, H. , "Radar CFAR thresholding in clutter and multiple target situations," IEEE Transactions on Aerospace and Electronic Systems, Vol. 19, 608-621, 1983.

[25] Y. Cui , G. Zhou , J. Yang and Y. Yamaguchi "On the iterative censoring for target detection in SAR images", IEEE Geosci. Remote Sens. Lett., vol. 8, no. 4, pp.641 -645 2011

[26] Everitt, B.S., Skrondal, A., "The Cambridge Dictionary of Statistics", second edition, Cambridge University Press, 2010

[27] Tao, D., S.N. Anfinsen and C. Brekke: Robust CFAR Dector based on Truncated Statistics in Multiple Target Situations, Geoscience and Remote Sensing, IEEE Transaction, In review, 44 pp.

[28] Q. H. Liu and N. Nguyen, "An accurate algorithm for nonuniform fast Fourier transforms (NUFFTs)", IEEE Microw. Guided Wave Lett., vol. 8, pp.18 -20 1998

[29] Gonzalez, R., Woods, R., "Digital Image Processing", third edition, Pearson Education, Inc., 2008

[30] Dong, Y., & Milne, A. K. (2001). Toward edge sharpening: a SAR speckle filtering algorithm. Geoscience and Remote Sensing, IEEE Transactions on, 39(4), 851-863.

[31] S. G. Dellepiane and E. Angiati, “Quality assessment of despeckled SAR images,” IEEE J. Sel. Topics Appl. Earth Obs. Remote Sens, vol. 7, pp.691 -707 2014

[32] Sheng, Y., & Xia, Z. G. (1996, May). A comprehensive evaluation of filters for radar speckle suppression. In Geoscience and Remote Sensing Symposium, 1996. IGARSS’96.’Remote Sensing for a Sustainable Future.’, International (Vol. 3, pp. 1559-1561).

IEEE.

[33] Commission I, W. G. WAVELET SPECKLE REDUCTION FOR SAR IMAGERY BASED ON EDGE DETECTION.

[34] H. Chunming, G. Huadong, and W. Changlin, “Edge preservation evaluation of digital speckle filters,” in IGARSS 2002, IEEE Int. Geosci. Remote Sensing Symp., Jun. 2002, vol. 4, pp. 2471–2473, 24-28

[35] Iqbal, M., Chen, J., Yang, W., Wang, P., & Sun, B. (2013). SAR image despeckling by selective 3D filtering of multiple compressive reconstructed images. Progress In Electromagnetics Research, 134, 209-226.

[36] Shamsoddini, A., Trinder, J. C., Wagner, W., & Székely, B. (2010). Image texture preservation in speckle noise suppression. na.

[37] Canny, J. (1986). A computational approach to edge detection. Pattern Analysis and Machine Intelligence, IEEE Transactions on, (6), 679-698.

[38] Fjortoft, R., Lopes, A., Marthon, P., & Cubero-Castan, E. (1998). An optimal multiedge detector for SAR image segmentation. Geoscience and Remote Sensing, IEEE Transactions on, 36(3), 793-802.

[39] Touzi, R., Lopes, A., & Bousquet, P. (1988). A statistical and geometrical edge detector for SAR images. Geoscience and Remote Sensing, IEEE Transactions on, 26(6), 764-773.

[40] Schou, J., Skriver, H., Nielsen, A. A., & Conradsen, K. (2003). CFAR edge detector for polarimetric SAR images. Geoscience and Remote Sensing, IEEE Transactions on, 41(1), 20-32.

[41] Walpole, Myers, Myers & Ye: "Probability and Statistics for Engineers and Scientists"; Ninth Edition, 2012, Pearson Prentice Hall.

[42] MATLAB documentation on fft2: www.mathworks.com/help/matlab/ref/fft2.html, April 2015

[43] Beylkin, G. (1995). On the fast Fourier transform of functions with singularities. Applied and Computational Harmonic Anal-

ysis, 2(4), 363-381.

[44] Hutchison, D., "Euro-Par 2010 - Parallel Processing: 16Th International Euro-Par Conference, Ischia, Italia, August/September 2010 Proceedings, Part 2", Springer, 2010

[45] Subiza, B., Gimeno-Nieves, E., Lopez-Sanchez, J. M., & Fortuny-Guasch, J. (2003, July). An approach to SAR imaging by means of non-uniform FFTs. In Geoscience and Remote Sensing Symposium, 2003. IGARSS'03. Proceedings. 2003 IEEE International (Vol. 6, pp. 4089-4091). IEEE.

[46] Keiner, J., Kunis, S., & Potts, D. (2009). Using NFFT 3–a software library for various nonequispaced fast Fourier transforms. ACM Transactions on Mathematical Software (TOMS), 36(4), 19.

[47] Fessler, J. A., & Sutton, B. P. (2003). Nonuniform fast Fourier transforms using min-max interpolation. Signal Processing, IEEE Transactions on, 51(2), 560-574.

[48] John Fessler - image reconstruction toolbox for MATLAB: http://web.eecs.umich.edu/~fessler/code/, April 2015

[49] Kunis, S. (2006). Nonequispaced FFT: generalisation and inversion. Shaker. Dissertation, University of Lübeck.

[50] Greengard, L., & Lee, J. Y. (2004). Accelerating the nonuniform fast Fourier transform. SIAM review, 46(3), 443-454.

[51] A. J. W. Duijndam and M. A. Schonewille, "Nonuniform fast Fourier transform", Geophys., vol. 64, no. 2, pp.539 -551 1999

[52] Steidl, G. (1998). A note on fast Fourier transforms for nonequispaced grids. Advances in computational mathematics, 9(3-4), 337-352.

[53] Kunis, S., & Potts, D. (2006). Time and memory requirements of the nonequispaced FFT. Techn. Univ., Fak. für Mathematik.

[54] Earth Observation Portal: https://directory.eoportal.org/web/eoportal/satellite-missions/r/radarsat-2

[55] MDA website:

http://gs.mdacorporation.com/SatelliteData/Radarsat2/Radarsat2.aspx

[56] Canadian Space Agency: http://www.asc-csa.gc.ca/eng/satellites/radarsat/radarsat-tableau.asp

[57] MDA Radarsat-2 Product Description: http://gs.mdacorporation.com/products/sensor/radarsat2/RS2_Product_Description.pdf

[58] NFFT 3.0 API Reference: https://www-user.tu-chemnitz.de/~potts/nfft/guide3/doc/structnfft__plan.html, May 2015

[59] Matlab documentation on Shepp-Logan phantom image: http://se.mathworks.com/help/images/ref/phantom.html, May 2015

[60] Eggers, H., Knopp, T., & Potts, D. (2007). Field inhomogeneity correction based on gridding reconstruction for magnetic resonance imaging. Medical Imaging, IEEE Transactions on, 26(3), 374-384.

[61] Daubechies, L. (1992). Ten lectures on wavelets (Vol. 61, pp. 198-202). Philadelphia: Society for industrial and applied mathematics.

[62] Valens, C., "A Really Friendly Guide to Wavelets", 1999

[63] Sweldens, W. (1998). The lifting scheme: A construction of second generation wavelets. SIAM Journal on Mathematical Analysis, 29(2), 511-546.

[64] Daubechies, I., Gustov, I., Schröder, P., & Sweldens, W. (1999). Wavelets on irregular point sets. Philosophical Transactions of the Royal Society of London. Series A: Mathematical, Physical and Engineering Sciences, 357(1760), 2397-2413.